

Fast matrix-free evaluation of discontinuous Galerkin finite element operators*

Martin Kronbichler[†] Katharina Kormann[‡]

November 13, 2017

Abstract

We present an algorithmic framework for matrix-free evaluation of discontinuous Galerkin finite element operators based on sum factorization on quadrilateral and hexahedral meshes. We identify a set of kernels for fast quadrature on cells and faces targeting a wide class of weak forms originating from linear and nonlinear partial differential equations. Different algorithms and data structures for the implementation of operator evaluation are compared in an in-depth performance analysis. The sum factorization kernels are optimized by vectorization over several cells and faces and an even-odd decomposition of the one-dimensional compute kernels. In isolation our implementation then reaches up to 60% of arithmetic peak on Intel Haswell and Broadwell processors and up to 50% of arithmetic peak on Intel Knights Landing. The full operator evaluation reaches only about half that throughput due to memory bandwidth limitations from loading the input and output vectors, MPI ghost exchange, as well as handling variable coefficients and the geometry. Our performance analysis shows that the results are often within 10% of the available memory bandwidth for the proposed implementation, with the exception of the Cartesian mesh case where the cost of gather operations and MPI communication are more substantial.

Key words. Matrix free method, Finite element method, Discontinuous Galerkin method, Sum factorization, Vectorization, Parallelization.

1 Introduction

The discontinuous Galerkin (DG) method gained a lot of momentum in a wide range of applications in the last two decades. The method combines the favorable features of the numerical fluxes in finite volume methods, often called Riemann solvers, with the high-order capabilities of finite elements based on polynomial bases. This construction allows for both high-order convergence rates on complicated computational domains as well as robustness in transport-dominated problems. DG methods have been identified as one of the most promising schemes for next-generation solvers in fluid dynamics and wave propagation problems and have also been introduced to a large number of other problems with mixed first and second order derivatives.

There is a large body of literature on implementing DG schemes and performance tuning for particular equations, especially for GPUs, see e.g. [26, 42, 1] and references therein. Classical matrix-based implementations for explicit time integration and various optimizations for triangles

*This work was supported by the German Research Foundation (DFG) under the project “High-order discontinuous Galerkin for the exa-scale” (ExaDG) within the priority program “Software for Exascale Computing” (SPPEXA), grant agreement no. KO5206/1-1 and KR4661/2-1. The authors acknowledge the support given by the Bayerische Kompetenznetzwerk für Technisch-Wissenschaftliches Hoch- und Höchstleistungsrechnen (KONWIHR) in the framework of the project *Matrix-free GPU kernels for complex applications in fluid dynamics*. The authors gratefully acknowledge the Gauss Centre for Supercomputing e.V. (www.gauss-centre.eu) for funding this project by providing computing time on the GCS Supercomputer SuperMUC at Leibniz Supercomputing Centre (LRZ, www.lrz.de) through project id pr83te.

[†]Institute for Computational Mechanics, Technical University of Munich, Boltzmannstr. 15, 85748 Garching b. München, Germany (kronbichler@lmm.mw.tum.de).

[‡]Max Planck Institute for Plasma Physics, Boltzmannstr. 2, 85748 Garching, Germany, and Zentrum Mathematik, Technical University of Munich, Boltzmannstr. 3, 85748 Garching, Germany (katharina.kormann@ipp.mpg.de).

and tetrahedra have reached a high level of maturity [19]. The focus of this work is on optimized shape value interpolation and derivative kernels for DG methods on quadrilaterals and hexahedra with moderate polynomial degrees in the range between 2 and 10 in the context of general meshes and variable coefficients. There exist special techniques for Cartesian meshes where the final cell matrix has tensor product structure [39, 21], but in the general case of more complex geometries and variable coefficient the final stencil cannot be separated into tensor products of 1D stencils. In that case, the fastest implementation option is usually the evaluation of integrals on the fly by fast sum factorization techniques [12, 24, 29] that have their origin in spectral elements [43, 44]. These methods have an operator evaluation cost of $\mathcal{O}(dk)$ per degree of freedom in the spatial dimension d for k polynomials per direction, i.e., polynomial degree $p = k - 1$, in contrast to costs of $\mathcal{O}(k^d)$ in matrix-based variants. While originally used for higher degrees, recent work [9, 34, 37] has shown that these techniques are up to an order of magnitude faster than sparse matrix kernels already for medium polynomial degrees of $p = 3$ or $p = 4$, with increasing gaps at higher orders.

Tensor product evaluation has been a very active research area with implementations available in the generic finite element software packages DUNE [8, 7], Firedrake [45, 41, 38], Loopy [25], mfem [27], Nek5000 [14], Nektar++ [10], or NGSolve [47] as well as application codes such as the compressible flow solver framework Flexi [20], SPECfEM3D [28] or pTatin3D [40]. Despite the wide availability of software, including code generators and domain-specific languages in Firedrake and Loopy, we believe that the analysis of high performance computing aspects and the expected performance envelopes of operator evaluation—independent of the user interfaces—are still missing. This work fills this gap by presenting an extensive analysis of the DG matrix-free operator evaluation with focus on the choice of data layouts and loop structures with their respective impact on performance for architectures with a deep memory hierarchy, supported by careful numerical experiments and results from hardware performance counters that quantify the effect of optimizations. Our focus is on three specific topics:

- efficient local kernels for shape value interpolation and derivatives with code vectorization over several elements,
- the storage of degrees of freedom with this vectorization scheme, and
- aspects of efficient MPI parallelization.

We concentrate on high-quality kernels for medium polynomial degrees $2 \leq p \leq 10$, but we show results also beyond this number to illustrate that there are no sudden breakdowns in performance. The proposed algorithms aim for reaching high single-node performance, but they also directly apply to the massively parallel context using the scheme presented in [6] as has been demonstrated on up to 147,456 cores in [37, 32], given that the communication in operator evaluation is only between nearest neighbors and thus naturally scalable to large processor counts. To the best of the authors’ knowledge, no similarly detailed analysis of DG algorithms for cache-based hardware has been previously presented in the literature. Selected well-performing options of the presented work are included in a comprehensive kernel collection of the open-source finite element library `deal.II` [3] and are accessible to generic applications within a toolbox providing other advanced features such as multigrid solvers and mesh adaptivity with hanging nodes. The developments in this work interoperate with the continuous finite element implementations from [34] using the same optimized code paths in the relevant algorithms and have already been used in a number of very challenging application codes in fluid dynamics [33, 32] and wave propagation [30, 36]. Note that operator evaluation is the central algorithmic part not only in explicit time integration but also for some implicit solvers such as multigrid methods with selected smoothers [11, 37].

This article is structured as follows. Sec. 2 introduces the mathematics of the underlying partial differential equations, the DG discretization, and the matrix-free implementation based on fast integration. Sec. 3 concentrates on the compute part of the algorithm, i.e., the tensor product kernels. The access to the solution vectors for cell and face integrals are analyzed in Sec. 4 alongside with the question of efficient ghost data exchange with MPI. Sec. 5 discusses the options for how to apply the geometry and Sec. 6 concludes this work.

2 DG algorithm

We assume a triangulation \mathcal{T}_h on the computational domain Ω that consists of a set of elements Ω_e . We denote the faces \mathcal{F}_h as the set of all intersections $\bar{\Omega}_{e^-} \cap \bar{\Omega}_{e^+}$, i.e., the edges of the cells in 2D and the surfaces of the cells in 3D, with the subset \mathcal{F}_h^i denoting the interior faces between two cells Ω_{e^-} and Ω_{e^+} with solution u_h^- and u_h^+ , respectively, and the set of boundary faces \mathcal{F}_h^b where only the solution field u_h^- is present. The vectors $\mathbf{n}^- = -\mathbf{n}^+$ denote the outer unit normal vectors on the two sides of a face. We also write \mathbf{n} instead of \mathbf{n}^- for the normal vector associated to the cell under consideration Ω_e .

The quantity $\{\{u\}\} = \frac{1}{2}(u_h^- + u_h^+)$ denotes the average of the values on the two sides of a face and the jump is written as $\llbracket u_h \rrbracket = u_h^- \mathbf{n}^- + u_h^+ \mathbf{n}^+ = (u_h^- - u_h^+) \mathbf{n}^-$. At domain boundaries, suitable definitions for the exterior solution u_h^+ in terms of the boundary conditions and the inner solution u_h^- are used, e.g. the mirror principle $u_h^+ = -u_h^- + 2g$ in case of Dirichlet conditions [19]. Inhomogeneous Dirichlet data add contributions to the right hand side vectors in linear systems.

To exemplify our algorithms and implementations, we consider two prototype discontinuous Galerkin discretizations to stationary problems: The DG discretization of the stationary advection equation with local Lax–Friedrichs (upwind) flux [19] is characteristic for first-order hyperbolic PDEs and reads

$$-(\nabla v_h, \mathbf{c} u_h)_{\Omega_e} + \left\langle v_h \mathbf{n}, \left\{ \{ \mathbf{c} u_h \} \right\} + \frac{|\mathbf{c} \cdot \mathbf{n}|}{2} \llbracket u_h \rrbracket \right\rangle_{\partial \Omega_e} = (v_h, f)_{\Omega_e}, \quad (1)$$

where $\mathbf{c} = \mathbf{c}(\mathbf{x})$ denotes the direction of transport and f is a forcing function. The bilinear form $(a, b)_{\Omega_e} = \int_{\Omega_e} ab \, d\mathbf{x}$ denotes volume integrals and $\langle a, b \rangle_{\partial \Omega_e} = \int_{\partial \Omega_e} ab \, d\mathbf{s}$ boundary integrals.

The symmetric interior penalty discretization of the Laplacian [4] is given by the weak form

$$(\nabla v_h, \nabla u_h)_{\Omega_e} - \left\langle \nabla v_h, \frac{1}{2} \llbracket u_h \rrbracket \right\rangle_{\partial \Omega_e} - \langle v_h \mathbf{n}, \{ \{ \nabla u_h \} \} \rangle_{\partial \Omega_e} + \langle v_h \mathbf{n}, \tau \llbracket u_h \rrbracket \rangle_{\partial \Omega_e} = (v_h, f)_{\Omega_e}, \quad (2)$$

on element Ω_e , containing the cell integral, the adjoint consistency term, the primal consistency term, and an interior penalty term with factor τ sufficiently large to render the discretization coercive.

Since the operators on the left hand sides of equations (1) and (2) are linear, they correspond to a matrix-vector product taking a vector of coefficient values $\mathbf{u} = [u_i]$ associated with the solution field u_h and returning the integrals $\mathbf{y} = [y_i]$ tested by test functions $v_h = \varphi_i$,

$$\mathbf{y} = \mathbf{A} \mathbf{u}. \quad (3)$$

Since our methods are based on numerical integration rather than the final cell matrices, the techniques extend straight-forwardly to nonlinear equations.

On each element Ω_e , we assume the solution to be given by an expansion $u_h^{(e)} = \sum_{i=1}^N \varphi_i(\mathbf{x}) u_i^{(e)}$, where $u_i^{(e)}$ are the coefficient values determined through the variational principle and $\varphi_i(\mathbf{x})$ are polynomial basis functions. For the definition of the integrals, we transform the basis functions on the reference element Ω_{unit} with coordinates $\boldsymbol{\xi}$ to the real element coordinates \mathbf{x} by a transformation $\hat{\mathbf{x}}^{(e)}$ as $\mathbf{x} = \hat{\mathbf{x}}^{(e)}(\boldsymbol{\xi})$ with Jacobian $\mathcal{J}^{(e)} = \frac{d\hat{\mathbf{x}}^{(e)}}{d\boldsymbol{\xi}} = \nabla_{\boldsymbol{\xi}} \hat{\mathbf{x}}^{(e)}$. Thus, the derivative can be expressed as $\nabla_{\mathbf{x}} \varphi(\boldsymbol{\xi}(\mathbf{x})) = (\mathcal{J}^{(e)})^{-T} \nabla_{\boldsymbol{\xi}} \varphi(\boldsymbol{\xi})$. In this work, we assume quadrilateral elements in 2D or hexahedral elements in 3D with shape functions defined through the tensor product of one-dimensional functions $\varphi_i(\xi_1, \xi_2, \xi_3) = \varphi_{i_1}^{1D}(\xi_1) \varphi_{i_2}^{1D}(\xi_2) \varphi_{i_3}^{1D}(\xi_3)$ with the respective multi-index (i_1, i_2, i_3) associated to the index i . The integrals in equations (1) and (2) are computed through numerical integration on a set of quadrature points $\boldsymbol{\xi}_q = (\xi_{q_1}, \xi_{q_2}, \xi_{q_3})$ with associated weights w_q defined as the tensor product of 1D quadrature formulas. For example, the cell term for advection in (1) is approximated by

$$\begin{aligned} (\nabla \varphi_i, \mathbf{c} u_h)_{\Omega_e} &= \int_{\Omega_{\text{unit}}} \left(\mathcal{J}^{(e)}(\boldsymbol{\xi})^{-T} \nabla_{\boldsymbol{\xi}} \varphi_i(\boldsymbol{\xi}) \right) \cdot \left(\mathbf{c} \left(\hat{\mathbf{x}}^{(e)}(\boldsymbol{\xi}) \right) u_h^{(e)}(\boldsymbol{\xi}) \right) \det(\mathcal{J}^{(e)}(\boldsymbol{\xi})) \, d\boldsymbol{\xi} \\ &\approx \sum_{q=1}^{n_q} \left(\mathcal{J}^{(e)}(\boldsymbol{\xi}_q)^{-T} \nabla_{\boldsymbol{\xi}} \varphi_i(\boldsymbol{\xi}_q) \right) \cdot \left(\mathbf{c} \left(\hat{\mathbf{x}}^{(e)}(\boldsymbol{\xi}_q) \right) u_h^{(e)}(\boldsymbol{\xi}_q) \right) \det(\mathcal{J}^{(e)}(\boldsymbol{\xi}_q)) w_q. \end{aligned} \quad (4)$$

2.1 Algorithm outline for discontinuous Galerkin finite element operator evaluation

The matrix-free evaluation of the integrals representing the product (3) is implemented by a loop over all the cells and faces appearing in the operators (1) or (2). The procedure for the advection operator (1) is outlined in Algorithm 1.

ALGORITHM 1: DG integration loop for the advection operator (1) with Dirichlet b.c.

- (i) **update_ghost_values:** Import vector values of \mathbf{u} from other MPI processes that are needed for computations of face integrals on the faces associated with the current process.
 - (ii) loop over cells
 - (a) gather local vector values $u_i^{(e)}$ on cell from global input vector \mathbf{u}
 - (b) interpolate local vector values $\mathbf{u}^{(e)}$ onto quadrature points, $u_h^{(e)}(\boldsymbol{\xi}_q) = \sum_i \varphi_i u_i^{(e)}$
 - (c) for each quadrature index j , prepare integrand in each quadrature point by computing $\mathbf{t}_q = \mathcal{J}^{(e)}(\boldsymbol{\xi}_q)^{-1} \mathbf{c}(\hat{\mathbf{x}}^{(e)}(\boldsymbol{\xi}_q)) u_h^{(e)}(\boldsymbol{\xi}_q) \det(\mathcal{J}^{(e)}(\boldsymbol{\xi}_q)) w_q$
 - (d) evaluate local integrals by quadrature $y_i^{(e)} = \left(\nabla \varphi_i, \mathbf{c} u_h^{(e)} \right)_{\Omega_e} \approx \sum_q \nabla \varphi_i(\boldsymbol{\xi}_q) \cdot \mathbf{t}_q$ for all test functions i
 - (e) write the local contributions $y_i^{(e)}$ into the global result vector \mathbf{y}
 - (iii) loop over interior faces
 - (a₋) gather local vector values u_i^- from global input vector \mathbf{u} associated with interior cell e^-
 - (b₋) interpolate u^- onto face quadrature points $u_h^-(\boldsymbol{\xi}_q)$
 - (a₊) gather local vector values u_i^+ from global input vector \mathbf{u} associated with exterior cell e^+
 - (b₊) interpolate u^+ onto face quadrature points $u_h^+(\boldsymbol{\xi}_q)$
 - (c) for each quadrature index j , compute the numerical flux contribution $(\mathbf{f}^* \cdot \mathbf{n}^-)_q = \frac{1}{2} \mathbf{c}(\hat{\mathbf{x}}^{(e)}(\boldsymbol{\xi}_q)) \cdot \mathbf{n}^- (u_h^-(\boldsymbol{\xi}_q) + u_h^+(\boldsymbol{\xi}_q)) + \frac{1}{2} \left| \mathbf{c}(\hat{\mathbf{x}}^{(e)}(\boldsymbol{\xi}_q)) \cdot \mathbf{n}^- \right| (u_h^-(\boldsymbol{\xi}_q) - u_h^+(\boldsymbol{\xi}_q))$ and multiply it by integration weight, $t_q = (\mathbf{f}^* \cdot \mathbf{n}^-)_q h(\boldsymbol{\xi}_q) w_q$ with area element h of face
 - (d₋) evaluate local integrals by quadrature $y_i^{e^-} = (\varphi_i^-, \mathbf{f}^* \cdot \mathbf{n}^-) \approx \sum_q \varphi_i(\boldsymbol{\xi}_q) t_q$
 - (e₋) add local contribution $y_i^{e^-}$ into the global result vector vector \mathbf{y} associated with e^-
 - (d₊) evaluate local integrals by quadrature $y_i^{e^+} = (\varphi_i^+, -\mathbf{f}^* \cdot \mathbf{n}^-) \approx \sum_q -\varphi_i(\boldsymbol{\xi}_q) t_q$ due to $\mathbf{n}^+ = -\mathbf{n}^-$ and the conservativity of the numerical flux function
 - (e₊) add local contribution $y_i^{e^+}$ into the global result vector vector \mathbf{y} associated with e^+
 - (iv) loop over boundary faces
 - (a) gather local vector values u_i^- from cell e^- from global input vector \mathbf{u}
 - (b) interpolate u^- onto face quadrature points $u_h^-(\boldsymbol{\xi}_q)$
 - (c) for each quadrature index j , compute the numerical flux contribution $(\mathbf{f}^* \cdot \mathbf{n}^-)_q = \left| \mathbf{c}(\hat{\mathbf{x}}^{(e)}(\boldsymbol{\xi}_q)) \cdot \mathbf{n}^- \right| u_h^-(\boldsymbol{\xi}_q)$ and multiply by integration factor, $t_q = (\mathbf{f}^* \cdot \mathbf{n}^-)_q h(\boldsymbol{\xi}_q) w_q$
 - (d) evaluate local integrals by quadrature $y_i^{e^-} = (\varphi_i^-, \mathbf{f}^*) \approx \sum_q \varphi_i(\boldsymbol{\xi}_q) t_q$
 - (e) add local contribution $y_i^{e^-}$ into the global result vector vector \mathbf{y} associated with e^-
 - (v) **compress:** Export parts of the residuals that have been generated on the current MPI process to the owning process.
-

Algorithm 1 is split into three phases, addressing the cell integrals, integrals for interior faces, and integrals for boundary faces in separate steps. Each of these loops logically consists of five components, which are (a) the extraction of the solution values pertaining to the current cell(s) by a gather operation, (b) the evaluation of values or gradients of the local solution in the quadrature points, (c) the operation on quadrature points including the application of the geometry, (d) the multiplication by the test functions and the summation in the numerical quadrature, and finally (e) accumulating the local values into the respective entry of the global vector by a scatter-add operation. Since each cell has independent degrees of freedom in DG, the algorithm can skip zeroing the result vector as typical in continuous finite elements [34] and instead set the integrals computed in the cell part (e), assuming that all relevant cell integrals are done before the respective face integrals.

In Algorithm 1, the steps (b) and (d) interpolating the solution from the coefficient values to quadrature points and quadrature loops are expensive in a naive implementation for higher polynomial degrees because all degrees of freedom inside a cell can contribute to the values on each quadrature point. For tensor product shape functions (or truncated tensors) on tensor product quadrature formulas, highly efficient schemes by sum factorization techniques as established in the spectral element community are available [43, 12, 24, 29].

Let us denote by S_i the $k \times k$ matrix of values of all k 1D shape functions of degree $p = k - 1$ evaluated in k quadrature points and by D_i the matrix of their derivatives along direction i , respectively. Further, denote by $\mathbf{u}^{(e)}$ the DG coefficients of the input vector. The evaluation of the d components of the gradient $\nabla_{\xi} u_h^{(e)}$ in d -dimensional space (step (b) of a variant of Algorithm 1 applied to the Laplacian and analogously for step (d) in transposed form) has the following Kronecker product form

$$\begin{bmatrix} D_1 \otimes S_2 \otimes \dots \otimes S_d \\ S_1 \otimes D_2 \otimes \dots \otimes S_d \\ \vdots \\ S_1 \otimes S_2 \otimes \dots \otimes D_d \end{bmatrix} \mathbf{u}^{(e)}, \quad (5)$$

and can therefore be implemented as a series of small matrix-matrix multiplications of dimension $k \times k$ for S_i and D_i and $k \times k^{d-1}$ for the coefficients. These operations can be interpreted as applying the matrices S_i and D_i along each coordinate direction for k^{d-1} lines. For evaluation of Eq. (5) in the collocation points, i.e., the case where quadrature points for nodal polynomials coincide with the node positions, the interpolation matrix is the $k \times k$ identity matrix, $S_i = I_i$. Omitting the calculations for interpolation is a classical optimization in spectral element codes [12, 29].

The collocation approach can be used to reduce cost of (5) also for other bases: if we define a 1D gradient matrix $(D_i^{\text{co}})_{q,j}$ as the gradient of Lagrange polynomials $\varphi_j^{\text{1D,co}}(\xi_q)$ with nodes in the quadrature points, i.e., $D_i = D_i^{\text{co}} S_i$, expression (5) can be rewritten as

$$\underbrace{\begin{bmatrix} D_1^{\text{co}} \otimes I_2 \otimes \dots \otimes I_d \\ I_1 \otimes D_2^{\text{co}} \otimes \dots \otimes I_d \\ \vdots \\ I_1 \otimes I_2 \otimes \dots \otimes D_d^{\text{co}} \end{bmatrix}}_{\text{collocation derivative}} \underbrace{[S_1 \otimes S_2 \otimes \dots \otimes S_d]}_{\text{basis change}} \mathbf{u}^{(e)}, \quad (6)$$

where the first multiplication $[S_1 \otimes S_2 \otimes \dots \otimes S_d] \mathbf{u}^{(e)}$ transforms the values $\mathbf{u}^{(e)}$ to the nodal basis defined in quadrature points. This transformation reduces the number of tensor product calls for the gradient from d^2 in (5) to $2d$ on general bases or $4dk^{d+1}$ arithmetic operations per cell. For comparison, a naive implementation that does not utilize the tensor product structure would involve $2dk^{2d}$ arithmetic operations. Integration is performed by multiplication with the transpose of the matrix in (6).

The interpolation matrix for face integrals is of similar form. For the case of the DG Laplacian that uses both function values and derivatives of u_h , face integration first interpolates values and gradients in normal direction to the face and then applies $(d-1)$ -dimensional tensor product operations. As an example, let us consider a face in 3D with normal in ξ_2 direction. The interpolation matrix consists of four blocks—the first block for the values in the quadrature points, the two subsequent blocks for the derivatives in the local coordinate direction of the face (ξ_1 and ξ_3 in this case), and the last block for the derivative in face-normal direction—and has the following structure

$$\underbrace{\begin{bmatrix} \begin{bmatrix} I_1 \otimes I_2 \\ D_1^{\text{co}} \otimes I_2 \\ I_1 \otimes D_2^{\text{co}} \\ 0 \end{bmatrix} [S_1 \otimes S_2] & 0 \\ 0 & [S_1 \otimes S_2] \end{bmatrix}}_{\text{interpolation within face}} \underbrace{\begin{bmatrix} I_1 \otimes S_f \otimes I_3 \\ I_1 \otimes D_f \otimes I_3 \end{bmatrix}}_{\text{face-normal interpolation}} \mathbf{u}^{(e)}, \quad (7)$$

where the $1 \times k$ matrices S_f and D_f evaluate the shape functions and their first derivative on the respective boundary of the reference cell. For derivatives in ξ_1 or ξ_3 directions the interpolation matrices are moved to the respective slots in the face-normal interpolation.

Remark 1 *Note that we do not consider the case where the final cell matrix (steps (b)–(d) in Algorithm 1) can be represented as a sum of Kronecker products, such as the Laplacian on a Cartesian geometry that has the form $L = L_1 \otimes M_2 + M_1 \otimes L_2$ in 2D. This involves fewer tensor product kernels than the numerical integration and can sometimes be further reduced in complexity [21]. These separable matrices only appear for the case of constant coefficients and axis-aligned meshes and are not the primary interest of this work, even though the presented sum factorization techniques can also be applied to that setting.*

2.2 Overview of algorithm design

Algorithm 1 has previously often been implemented by specializations for the particular equations at hand or selected parallelization schemes in the high performance community, which have been discussed in an enormous body of literature on DG methods. This work attempts a systematic approach to identify implementations that combine generic software interfaces in C++ not tied to a particular equation with high performance execution.

The vector access steps (a) and (e) in Algorithm 1 only shuffle around memory and are thus memory bandwidth bound when considered in isolation. Conversely, the interpolation and integration steps (b) and (d) in Algorithm 1 repeatedly go through a limited set of data in different orders and allow for caching: the data extracted from the input vector is combined with the coefficients of the polynomial evaluation to some intermediate arrays holding the data on all quadrature points, see Sec. 3. The operations performed in quadrature points, step (c) in the algorithm, have most variability and depend on the differential operator and the user code as discussed in Sec. 5. In order to assess the effects of code optimizations separately, the following three sections discuss one of the aspects with idealized implementations of the other steps of Algorithm 1. Note that the presented optimization techniques do not interact with each other in the chosen order, so they can be derived one after another.

Given this initial characterization, it is clear that the memory-intensive operations in the vector access and the geometry stages should be mixed with the compute-dominated interpolation and integration steps such that the data that flows between the different phases in the algorithm remains in cache memory as much as possible and prefetchers can pre-load vector entries or coefficients during compute phases. Thus, implementations must perform all operations of a cell or a few cells together with a single outer loop. For instance, a copy of the vector data into formats more amenable to vectorization or basis change operations should be done local to a few cells unless all data fits into the last-level caches. Along the same lines, the overall operator evaluation often performs best when interleaving the cell loop (ii) with the inner face loop (iii) and the boundary face loop (iv) in Algorithm 1 because they can re-use the vector entries in caches.

3 Performance-driven design of sum factorization kernels

In this section, we start by an analysis of the sum factorization kernels for cell integrals which have a complexity of $\mathcal{O}(k)$ per degree of freedom. To eliminate memory effects, we apply the kernels to data corresponding to a single cell (or a batch of cells when vectorizing) throughout this section. This data is repeatedly accessed in an outer loop whose length is set to reach a benchmark run time of a few seconds. To give a more realistic picture of application performance, we run the full cell operation stage (b)–(d) in Algorithm 1 including the loop over quadrature points that applies the geometry, without artificially looking at the sum factorization step only. In particular, our numbers include the cost of selecting between different code paths for curved or affine geometries according to [34].

Our performance experiments are based on the three Intel-based HPC systems presented in Table 1, including two server processors and a throughput-oriented Xeon Phi. We have verified that benchmarks were run at the maximum AVX frequency given in the table, and report all timings as the average of runs over at least a few seconds after a warm-up period of a few minutes to represent as fair performance numbers as possible. As a compiler we use the GNU compiler `g++` of version 6.3.0 with flags `-O3 -funroll-loops -march=native` that in our case generates executables of slightly better performance than `clang` 3.9.0 and the Intel compiler version 16 and 17.

Table 1: Specification of hardware systems used for evaluation. Memory bandwidth according to the STREAM triad benchmark and GFLOP/s based on theoretical maximum at AVX turbo frequencies.

	Haswell Xeon E5-2630 v3	Broadwell Xeon E5-2690 v4	Knights Landing Xeon Phi 7120
cores	2×8	2×14	64
frequency base	2.4 GHz	2.6 GHz	1.3 GHz
max AVX turbo frequency	2.6 GHz	2.9 GHz	1.1 GHz
SIMD width	256 bit	256 bit	512 bit
arithmetic peak @ AVX turbo	666 GFLOP/s	1299 GFLOP/s	2253 GFLOP/s
last level cache	2.5 MB/core L3	2.5 MB/core L3	512 kB/core L2
memory bandwidth	95 GB/s	112 GB/s	450 GB/s (MCDRAM)

The Haswell system with 2×8 cores is a system with relatively high memory throughput as compared to arithmetics. The Broadwell system with 2×14 cores at 2.6 GHz has almost twice the core count and theoretically offers twice the arithmetic performance of the Haswell system, but with the same number of 8 DDR4 memory channels and only slightly higher STREAM memory throughput due to a higher memory clock rate. The Knights Landing Processor has 64 cores that run with wider vector units but at a low frequency of 1.3 GHz and with reduced features, the most important of which are the only 2-wide decode throughput and the absence of a level-3 cache.

3.1 Tensor product algorithms

The summations in the interpolation kernel according to Eq. (6) and its transpose for integration as used in Algorithm 1 involve a series of small matrix-matrix multiplications and are the dominating factor for reaching high performance. Due to the small dimensions of the matrices of $k \times k$ for the coefficient array and $k \times k^2$ for the 3D solution values, generic BLAS multiplication kernels `dgemm` that are specialized for the LINPACK context of medium and large sizes are not suitable due to large function call and dispatch overheads. As an alternative, optimized small matrix multiplication kernels have been suggested by the batched BLAS initiative [13] and by the `libxsmm` project [16]. However, these interfaces potentially lose some of the context of the repeated matrix multiplications along different directions, i.e., with different strides, leading to additional load/store operations between registers and the L1 cache that are often the limit for throughput. Also, separating the tensor product kernels from the quadrature loop and vector access as assumed by batched BLAS [13] sacrifices data locality and thus performance in the low and medium polynomial degree case. Instead, this setting is best handled by an optimizing compiler in our experience. Obviously, enough information about the loops and data arrays must be given to the compiler to ensure generation of good machine code. As we will show below, very good numbers can indeed be obtained with compiled C++ code when letting the compiler choose the loop unrolling and register allocation, but forcing the use of full SIMD vectors by intrinsics.

For the steps (b) and (d) in Algorithm 1, we consider three compute kernels, `basis_change`, `collocation_derivative`, and `face_normal_interpolation`. Before discussing their optimization, let us briefly introduce the properties of the kernels and their signature.

```
template <int d, bool interpolate, int k, int l, bool add, typename Number>
void basis_change(const Number* shape_values, const Number* in, Number* out)
```

The `basis_change` kernel implements the change between different polynomial bases in d space dimensions. It involves d tensor product sweeps passing through each dimension according to the matrix $[S_1 \otimes S_2 \otimes \dots \otimes S_d]$ in Eq. (6), with the array `shape_values` storing the entries of the S matrices. The boolean template argument `interpolate` selects either the interpolation or the integration path. The algorithm is generic, though, and the switch between interpolation and integration is merely between interpreting the shape value array as either row-major or column-major. The 1D size of the two bases is given by k on the degree of freedom dimension and l on the quadrature dimension, respectively. Well-defined interpolation must satisfy $k \leq l$, i.e., interpolate to a basis of the same degree or a higher degree. The boolean template argument `add` defines whether the result should be added into the output array or overwrite previous content. This

Table 2: Number of calls to tensor product kernels in d dimensions for the advection operator with a Lagrange basis on Gauss–Lobatto points and the Laplacian on a Hermite-type basis using Gaussian quadrature on k^d points. The basis change and derivative columns specify how the total number of sum factorization kernels is derived.

	total no. of kernels	basis change	derivative	face normal
advection GL, cell	$3d$ on k^d pts	$2d$	d	—
advection GL, inner face	$4d$ on k^{d-1} pts	$4(d-1)$	—	4 on k^{d-1} pts
advection GL, boundary face	$2d$ on k^{d-1} pts	$2(d-1)$	—	2 on k^{d-1} pts
Laplacian Hermite, cell	$4d$ on k^d pts	$2d$	$2d$	—
Laplacian Hermite, inner face	$12(d-1)$ on k^{d-1} pts	$8(d-1)$	$4(d-1)$	8 on $2k^{d-1}$ pts
Laplacian Hermite, bdry face	$6(d-1)$ on k^{d-1} pts	$4(d-1)$	$2(d-1)$	4 on $2k^{d-1}$ pts

is used when adding the local results of an integral into previous content in a global vector, for instance. The result can be stored in place if the data along the 1D input stripe is held in registers while passing through the rows of the 1D interpolation matrix and appropriate order through the input array. The number type `Number` is either a simple scalar like `double` or a more complicated SIMD type that we call `VectorizedArray<double>` or `VectorizedArray<float>` with overloaded arithmetic operations.

For a mass matrix evaluation or an inverse mass matrix evaluation according to [36], the basis change kernel is first applied in the `interpolate=true` version, the determinant of the Jacobian and the quadrature weights are applied in each quadrature point (multiplication by a diagonal matrix), and integration is performed by calling the kernel with `interpolate=false`, using the same `shape_values` array as for interpolation.

```
template <int d, bool interpolate, int k, bool add, typename Number>
void collocation_derivative(const Number* shape_derivatives, const Number* in,
                          Number* out)
```

The `collocation_derivative` kernel implements the unit-cell derivative in collocation space according to the left matrix in Eq. (6) using d tensor product kernel invocations on k^d points each. If `interpolate==true`, d components of the gradient are created from a single input field, whereas d consecutive fields are summed together if `interpolate==false`.

For evaluating the unit-cell gradient according to Eq. (6) on an arbitrary basis, the two kernels `basis_change` and `collocation_derivative` are applied sequentially for the same cell batch, involving $2d$ tensor product kernels. Of course, our algorithm design can bypass `basis_change` for collocation of nodal points and quadrature points. Algorithms similar to `basis_change` and `collocation_derivative` were already proposed in [29] but without discussion of their properties of modern hardware.

```
template <int d, int direction, bool interpolate, int k, int highest_derivative,
          typename Number>
void face_normal_interpolation(const Number* shape_matrix, const Number* in,
                              Number* out)
```

This kernel implements the interpolation of values and gradients in face-normal direction (right part of Eq. (7)) when passing either S_f or D_f as `shape_matrix`. It contains short-cuts for special polynomial bases where most of the entries in S_f and D_f are zero: If only a single entry in $S_f \in \mathbb{R}^{1 \times k}$ is non-zero, only k^{d-1} coefficient values contribute to the interpolation on the face (`nodal_on_faces`). Likewise, a Hermite-type basis (`hermite_type_basis`) where at most two entries in both S_f and D_f are nonzero, respectively, allows to compute values and derivatives from only $2k^{d-1}$ coefficients. This functionality can be integrated with the vector access functions according to Sec. 4 below to skip reading the remaining vector entries. The interpolation and integration steps (b) and (d) within the face are performed by combining the `face_normal_interpolation` kernel with the $(d-1)$ -dimensional version of the `basis_change` and `collocation_derivative` functions. All components of face integrals involve only $\mathcal{O}(1)$ arithmetic operations per cell degree of freedom. They reduce in complexity against cell integrals at higher convergence orders k and we postpone the analysis of face integrals to subsection 3.5.

Table 2 specifies the number of tensor product invocations when calling Algorithm 1 for the advection operator on the left hand side of (1) and the respective algorithm for the left hand

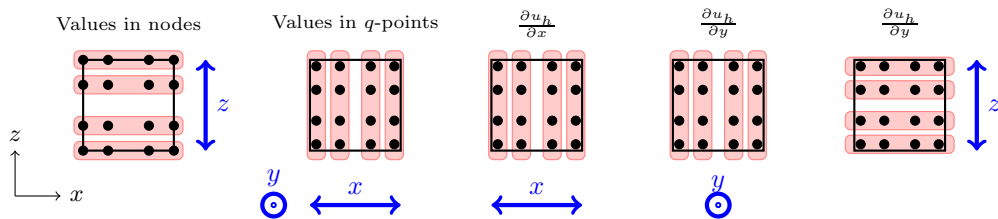


Figure 1: Visualization of a possible vectorization scheme within a single element shown in $x - z$ plane with y -direction orthogonal to the sketch. Red shaded symbols denote the entries within a single SIMD array, involving transpose (cross-lane) operations to switch from one order to the other. Blue arrows show the action of 1D interpolations, one arrow per tensor product invocation.

side of the Laplacian (2). A nodal basis on Gauss–Lobatto points and a Hermite-like basis, respectively, are chosen such that the operator evaluation time is minimal for polynomial degrees up to 10. We explicitly note that the operator evaluation with the collocation basis executes more slowly on an actual implementation despite fewer tensor product calls. This is because `face_normal_interpolation` must access all k^d points of a cell rather than only the $2k^{d-1}$ with non-zero value and first derivative on the face. A comparative analysis will be performed in a subsequent contribution. The table reports the total number of tensor product kernels for both the interpolation step (b) and the integration step (d). The higher order of the derivatives in the Laplacian imply more work, in particular for the face integrals where both the values and the gradients must be computed from Eq. (7). In Table 2, we count the interpolation of the values and normal derivatives as two invocations to a face normal interpolation to quantify the increased cost, even though they are implemented by a single pass through the data.

3.2 Vectorization strategy

Modern high-performance CPU architectures increasingly rely on single-instruction/multiple-data (SIMD) primitives as a means to improve performance per watt. In short-vector SIMD, a single arithmetic or load/store operation is issued to process a number of n_{lanes} data elements with the same instruction independently. Cross-lane permutations require separate instructions that may incur a performance penalty, depending on the superscalar execution capabilities of the microarchitecture. Furthermore, loads and stores are faster if accessing a contiguous range of memory (packed operation) as compared to indirect addressing with `gather` or `scatter` instructions with multiple address generation steps.

A first, most obvious, option is to vectorize within a cell clustering 1D slices of the degrees of freedom. For sum factorization, this is intriguing because the 1D kernels go through data in different orders for each dimension. As visualized in Fig. 1, three lane-crossing transpose operations of length k^d are needed in the spirit of array-of-struct into struct-of-array conversions. In case the number of 1D degrees of freedom is not a multiple of the SIMD width, one needs to fill up the last SIMD array along that direction with dummy values, which leads to distinct drops in the performance. Alternatively, smaller SIMD widths could be used for the remainder parts.

The second option, which is preferable in our experience, is to vectorize over several cells. Fig. 2 shows a numbering of degrees of freedom on a \mathcal{Q}_3 basis in 2D with 4-wide vectorization which allows for direct packed access. In this layout, the lower left node values of four cells are placed adjacent in memory. The next storage location is the second node for all four cells, and so on. In this format, no cross-lane data exchange is needed for cell integrals and the sum factorization kernels can be directly called on the data stored in the global input vector without a separate gather step. When vectorizing over several cells, all arithmetic operations can be performed straightforwardly, including the various tensor product kernels and the operations in quadrature points, by using overloaded SIMD data types according to [34, 35]. Furthermore, this scheme can straightforwardly select the most beneficial width of vectorization for a given hardware. Partially filled lanes occur at most on a single element batch per operator evaluation and MPI rank for meshes whose number of cells is not divisible by the vectorization width. We also apply this approach to face integrals, i.e., we process the integrals of several faces at once, rather than SIMD-parallelizing

e_3				e_4				e_7				...
50	54	58	62	51	55	59	63	114	118	122	126	...
34	38	42	46	35	39	43	47	98	102	106	110	...
18	22	26	30	19	23	27	31	82	86	90	94	...
2	6	10	14	3	7	11	15	66	70	74	78	...
e_1				e_2				e_5				...
48	52	56	60	49	53	57	61	112	116	120	124	...
32	36	40	44	33	37	41	45	96	100	104	108	...
16	20	24	28	17	21	25	29	80	84	88	92	...
0	4	8	12	1	5	9	13	64	68	72	76	...

Figure 2: Visualization of layout of degrees of freedom for vectorization over elements, using a typical array-of-structure-of-array data structure.

within a face or over the two cells adjacent to a face.

In order to maintain data locality, we finish all operations of steps (a)–(e) in Algorithm 1 on a batch of cells, e.g. the cells indexed by $\{e_1, e_2, e_3, e_4\}$ in Fig. 2, before proceeding with the next batch of cells, e.g. cells $\{e_5, e_6, e_7, e_8\}$. Besides requiring a change in the loop over the mesh, two possible disadvantages of this scheme are

- a somewhat larger spread in the indices of gather/scatter steps of face integrals,
- cases where the number of elements per MPI task is less than the width of vectorization do not see speedups, which is usually only limiting over the communication cost for more than 500 degrees of freedom per cell [37], and
- a larger active size of the temporary arrays in sum factorization, which might exceed the capacity of caches and thus slow down execution. In the following, we show that this issue is uncritical in the common context of $p < 15$, i.e., $k < 16$.

The performance of the two vectorization variants, implemented through wrappers around intrinsics, is shown in Fig. 3. The figure also contains data points with automatic vectorization as exploited by the GNU compiler with `_restrict` annotations to arrays to help the compiler in the aliasing analysis. Vectorization over several cells clearly outperforms vectorization within a single cell for low and moderate polynomial degrees $1 \leq p \leq 10$. While the former shows an approximately linear degradation of performance due to the complexity $\mathcal{O}(p + 1)$ in the cell integrals, the latter increases throughput as the lanes get more populated, with sudden drops in performance once an additional lane must be used at $p = 4, 8, 12, 16, 20, 24$. The automatic vectorization is not competitive, with a performance disadvantage of a factor 2.1 to 3.7 (average in 3D: 3.1) with 4-wide vectorization. This is because only 5% to at most 25% of arithmetic instructions are done in packed form.

In order to improve data locality of the sum factorization, Algorithm 2 proposes to merge loops over x and y within a single loop over the last direction z . This exploits the natural cache blocking of tensor products and is particularly useful for vectorization over several cells which have a larger local data set than the scalar variant. The corresponding data point is marked as “vectorized over cells tiled” in Fig. 3.

Further details on the kernel variants are provided by a cache access analysis that repeatedly runs through the kernels on a single batch of cells. Fig. 4 shows measurements of the actual data transfer (read + evict) between the various cache levels of an Intel Haswell Xeon E5-2630 v3 with 4-wide vectorization extracted from hardware performance counters with the `likwid`¹ tool with `likwid-mpirun -n 16 -g CACHES` to populate all 16 cores of the system. Raising the polynomial degree increases the size of the temporary arrays holding intermediate results of sum factorization as expected. For vectorization over cells, degrees larger than 5 start spilling to L2 cache and degrees larger than 10 spill to L3 cache. The tiled algorithm cuts data access into a half to a third

¹<https://github.com/rrze-hpc/likwid>, retrieved on May 20, 2017.

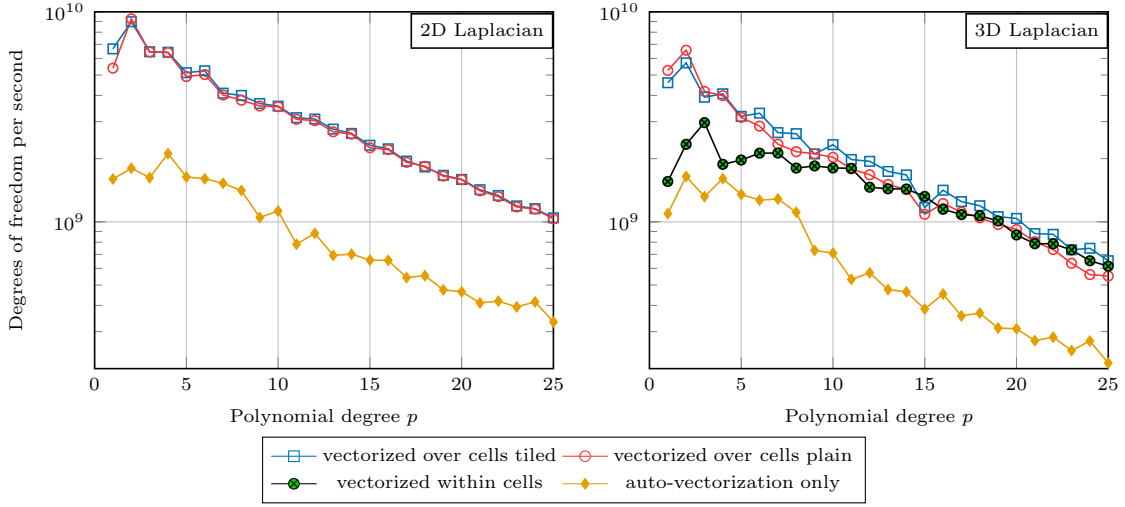


Figure 3: Comparison of throughput of local cell kernels on fully populated 2×8 cores Intel Haswell (Xeon E5-2630 v3 @ 2.4 GHz) for cell integrals with respect to vectorization for Laplacian in 2D and 3D.

ALGORITHM 2: Loop tiling for sum-factorized evaluation of the cell Laplacian in 3D

- for $i_z = 0, \dots, k-1$
 - Kernel for S_1 along x for k^2 points in xy plane with offset $(i_z - 1)k^2$ and stride 1
 - Kernel for S_2 along y for k^2 points in xy plane with offset $(i_z - 1)k^2$ and stride k
 - for $i = 0, \dots, k^2 - 1$
 - Kernel for S_3 along z for k points with offset i and stride k^2
 - Kernel for D_3^{co} along z for k points with offset i and stride k^2
 - for $i_z = 0, \dots, k-1$
 - Kernel for D_2^{co} along y for k^2 points with offset $i_z k^2$
 - for $i_y = 0, \dots, k-1$
 - * Kernel for D_1^{co} along x for k points with offset $i_z k^2 + i_y k$
 - * Apply Laplacian on k quadrature points along x direction with offset $i_z k^2 + i_y k$ according to step (c) of Algorithm 1.
 - * Kernel for $(D_1^{\text{co}})^{\text{T}}$ (integration) along x for k points with offset $i_z k^2 + i_y k$
 - Kernel for $(D_2^{\text{co}})^{\text{T}}$ along y for k^2 points with offset $i_z k^2$; sum into result from x direction
 - for $i = 0, \dots, k^2 - 1$
 - Kernel for $(D_3^{\text{co}})^{\text{T}}$ along z for k points with offset i ; sum into results from x, y directions
 - Kernel for S_3^{T} along z for k points with offset i and stride k^2
 - for $i_z = 0, \dots, k-1$
 - Kernel for S_2^{T} along y for k^2 points in xy plane with offset $i_z k^2$ and stride k
 - Kernel for S_1^{T} along x for k^2 points in xy plane with offset $(i_z - 1)k^2$ and stride 1
-

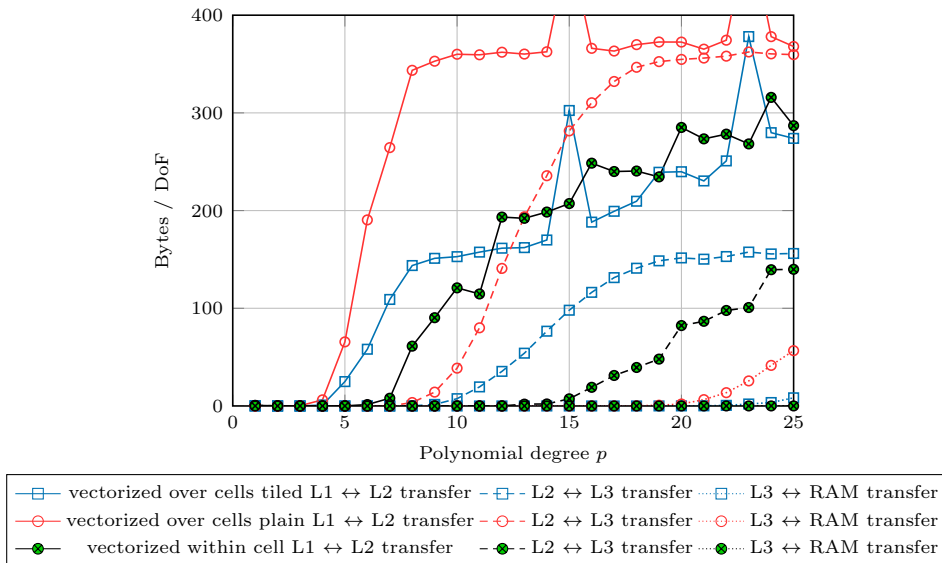


Figure 4: Memory access per degree of freedom on various levels of the memory hierarchy for the compute part of the 3D Laplacian run on all cores of an Intel Haswell Xeon E5-2630 v3.

for larger polynomial degrees because data is aggregated along 2D planes. For vectorization within cells, the active set is smaller by a factor of four approximately, and spilling to L1 only starts at degree 8 and spilling to L3 cache gets significant only for degrees larger than 20.

However, the reduced transfer from caches when vectorizing within cells does not materialize in better performance. This is because more transfer from outer level caches comes along with more arithmetics due to the linear increase in work according to the complexity $\mathcal{O}(k)$ per DoF, nicely offsetting the reduced throughput and increased latency of outer level caches. When compared to the access to L1 cache which is around 800–2000 Bytes/DoF (larger numbers for larger degrees), access of up to 400 Bytes/DoF hitting the L2 cache is uncritical for vectorization over cells: the L2 cache can sustain about half to one third of the throughput of the L1 cache [22]. Likewise, throughput of the L3 cache is around half that of L2 cache in recent Intel architectures, which is again a nice fit with the access patterns in sum factorization according to Fig. 4 (square symbols).

Vectorization within cells only becomes superior beyond $k = 21$ in 3D where already the size of the local vector data is 21^3 [DoFs per cell] \times 32 [Bytes/AVX SIMD] = 296 kiB and thus exceeds the level 2 cache on Intel processors with AVX vectorization. The only apparent outlier is degree 15 with $k = 16$ on 16^3 degrees of freedom per cell which is affected by cache associativity limitations due to access to 64 entries at a distance of exactly 8 kiB = 256×32 [Bytes] in between.

Design Choice 1 *In operator evaluation, quadrature point operations according to step (c) in Algorithm 1 can take a substantial amount of time compared to sum factorization, in particular for face integrals. To obtain optimal performance, vectorization must also be applied to the operation in the quadrature points. Vectorization can be encapsulated in user code by vectorized data types and operator overloading.*

3.3 Optimization of loop kernels

When it comes to the actual implementation of the small matrix-matrix product loop kernels, several optimizations steps beyond a basic loop implementation that passes the loop bounds as run time variables are selected in our implementation. Fig. 5 compares these optimizations in terms of the number of degrees of freedom processed per second when working on all cores of the 2×8 Intel Haswell system. The vectorization over elements as presented in the previous subsection is used, without the tensor-product tiling to ease the implementation of register blocking schemes.

- **Template parameter on loop bounds.** This optimization is essential for the short loops at small polynomial degrees, as it allows the compiler to completely unroll the loops and to

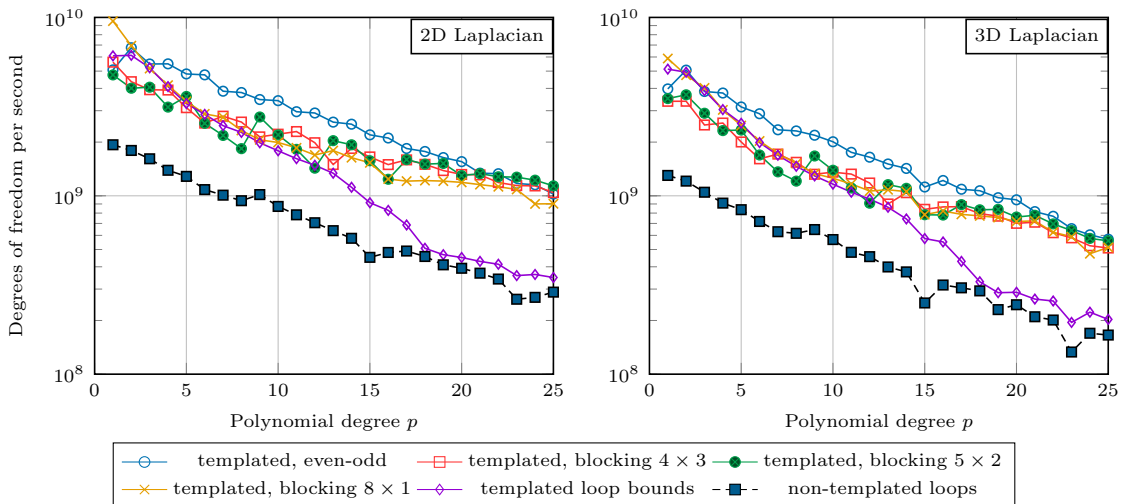


Figure 5: Analysis of implementation of matrix multiplication kernels on throughput of local Laplace cell kernels on fully populated 2×8 cores Intel Haswell (Xeon E5-2630 v3 @ 2.4 GHz) in 2D and 3D. The standard matrix-matrix multiplication loops are provided in four variants, three of which use register blocking with $r \times s$ accumulators, running through r local shape value rows and s layers of shape values.

re-arrange operations to improve instruction flow. Fig. 5 shows that performance increases by a factor of three approximately. We found best performance when keeping the data input along a one-dimensional line of the data array in registers and loading the entries in the 1D interpolation matrix from L1 cache of full vectorization width.

- For higher degrees, the compiler’s heuristics do not generate optimal matrix multiplication code from the templated loops alone. Throughput is considerably improved by **loop unrolling and register blocking** as classically used in state-of-the-art matrix-matrix multiplication `gemm` kernels and appearing in `libxsmm` [16]. For the reported results, we manually apply 4×3 , 5×2 , and 8×1 unrolling with 12, 10 and 8 independent accumulators, with the first number referring to the blocking within the coefficient matrix and the second number the lines along which blocking is applied. At low degrees where not enough data streams are available for blocking, appropriate remainder code is generated. The 5×2 blocked variant reaches up to 500 GFLOP/s in 2D (75% of the theoretical peak of 666 GFLOP/s at maximal AVX turbo) for degrees between 13 and 25 and up to 420 GFLOP/s for degrees 9, 14, and 19 in 3D (60% of arithmetic peak).
- **Even-odd decomposition of local matrix-vector kernels.** For the case that integration points are symmetric, shape functions symmetric, and derivatives skew-symmetric with respect to the center of the cell, there are only $k^2/2$ unique entries of the k^2 total entries in the 1D interpolation or derivative matrices. Thus, working separately on the even and odd components of the vector [29, Sec. 3.5.3] reduces the operation count for a one-dimensional kernel from $k(2k - 1)$ arithmetic operations (k multiplications, $k(k - 1)$ fused multiply-add operations, FMAs) to

$$2k \text{ additions/subtractions, } k \text{ multiplications, and } \lfloor k(k - 2)/2 \rfloor \text{ FMAs,} \quad (8)$$

where the additions and subtractions are spent on adding and subtracting the first and last vector entries, the second and the second to last, and so on, to extract the even and odd parts of the vector. Besides reducing arithmetics, the even-odd decomposition also provides for a natural 2×1 loop unrolling. The experiments show a significantly higher performance that is more regular than the various loop blocking approaches with the full matrix. As reported in Fig. 6 below, the GFLOP/s go down to around 350 GFLOP/s as compared to the full matrix multiplication, but the GFLOP/s rates are secondary quantities anyway. At very high degrees, $p > 20$, the even-odd implementation could be enhanced by further blocking.

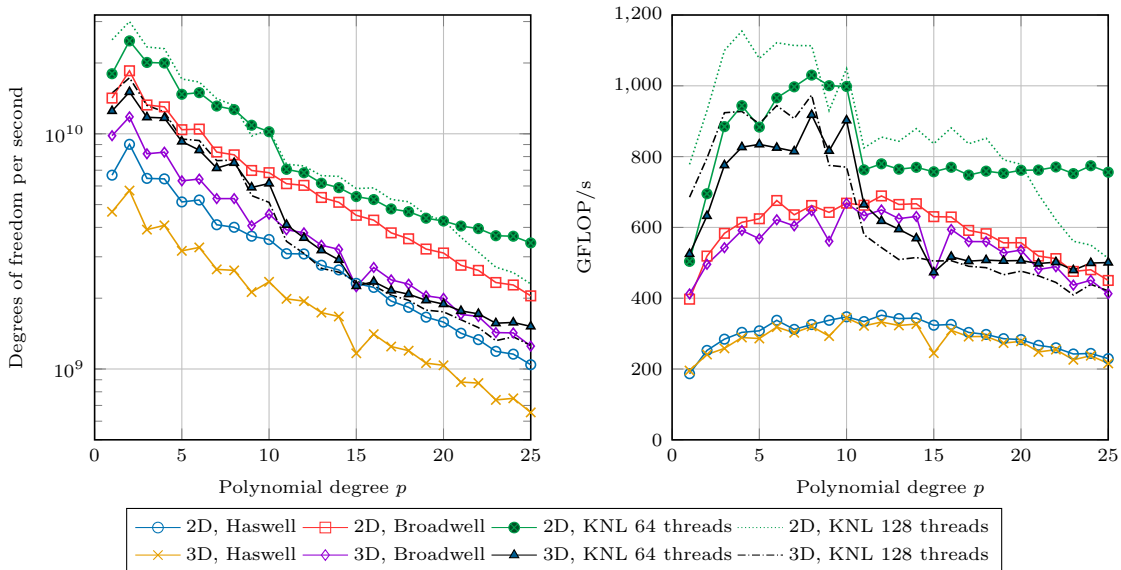


Figure 6: Throughput of local cell kernels on 2×8 core Intel Xeon E5-2630 v3 (Haswell), 2×14 core Intel Xeon E5-2690 v4 (Broadwell), and 64 core Intel Xeon Phi 7210 (KNL) for cell integrals of Laplacian in 2D and 3D.

3.4 Compute performance on CPUs and Xeon Phi

We now analyze the throughput of the best kernel for the cell Laplacian, invoking $2d$ tensor product kernels in two `basis_change` calls and $2d$ tensor product kernels in two `collocation_derivative` calls according to Table 2, each implemented with even-odd decomposition with loop tiling and templated loop bounds, on the three Intel processors presented in Table 1.

Fig. 6 shows that the Haswell system reaches 340–350 GFLOP/s in both 2D and 3D around $p = 10$. The number of floating point operations is obtained by multiplying the cost per tensor product kernel from Eq. (8) by $4d$, the number of calls to tensor product kernels according to Table 2, and including the cost per quadrature point on a Cartesian mesh involving $2d + 1$ multiplications. We have verified that these numbers are accurate to within 10% of the measured arithmetic throughput with `likwid`. For the mix of additions, multiplications, and FMAs in the even-odd kernel according to Eq. (8), the throughput ceiling can be computed to be 340 GFLOP/s for $p = 1$, 465 GFLOP/s for $p = 3$, 550 GFLOP/s for $p = 5$ and approaching 600 GFLOP/s for $p = 20$. In other words, the code reaches up to 40–60% of the possible arithmetic performance.² Also, the actual performance limit is often the L1 cache read and write access rather than pure arithmetics. On Broadwell, the best performance is 690 GFLOP/s in 2D and 670 GFLOP/s in 3D, again up to 60% of the possible arithmetic throughput assuming *highest AVX turbo* for the actual upper range of between 700 and 1150 GFLOP/s. As expected, we reach similar percentages of the arithmetic peak on both Haswell and Broadwell because the test case is compute only. Given that our code reaches more than 50% of FMA peak with the even-odd decomposition, it outperforms any version of straight matrix multiplication as documented in Fig. 5. Similar GFLOP/s rates are achieved in the mass matrix application (at twice the DoF/s throughput) and the advection operation (at 1.5 times the DoF/s throughput).

On the KNL many-core processor, the gap to the theoretical value of 2250 GFLOP/s is larger. In 3D, a decrease in arithmetic performance is observed for $p \approx 11$ where the inner kernel exhausts the 512 kiB of L2 cache per core and an increasingly larger part of the local integration data needs to be fetched from the MCDRAM memory. Note that performance for $p > 10$ is only around 50 GFLOP/s when binding the kernel to the slow DDR4 RAM with `numactl --mbind=0` rather than the fast 16 GB of MCDRAM [23]. The tensor product tiling of Algorithm 2 and the generated machine code are more important on KNL than on the CPUs and in particular once the

²Performance is sensitive to the compiler’s choices in register allocation and loop unrolling. For example, we recorded `g++` of version 7.1 to be 10% slower on $p = 8$ than `g++` version 6.3, but almost equal for many other degrees.

L2 cache is exceeded. For example, the jump between degrees 10 and 11 in 2D is due to machine code generation effects, with the whole 1D input line of sum factorization fitting into registers for $p \leq 10$ and re-loading them for higher degrees. Furthermore, we observe considerably lower GFLOP/s rates in 3D than in 2D, as opposed to the Haswell and Broadwell systems, which could be explained by more loads and stores from caches as compared to arithmetics in 3D. Nonetheless, our results show that one can reach around 1 TFLOP/s for low to moderate polynomial degrees or 50% of peak arithmetic performance, which is extremely good given the restricted hardware features of the KNL microarchitecture. Note that for low degrees $p \leq 7$ in 3D and for $p \leq 20$ in 2D, KNL with two-way simultaneous multithreading (128 threads) performs better than on 64 threads, but the picture is reversed for higher degrees when too much local data is in flight.

3.5 Compute throughput of cell and face integrals

Finally, we include face integrals in the comparison. In order to efficiently evaluate face integrals, we use a nodal basis for advection with the nodes of the k -point Gauss–Lobatto–Legendre quadrature formula, i.e., one node placed at each of the 1D interval endpoints. This allows to directly pick the k^{d-1} node values on the face without interpolation normal to the face over all k^d points. Likewise, a Hermite-like basis is chosen for the Laplacian (2) that can compute the solution’s value and derivative on the face from $2k^{d-1}$ solution values on cubic and higher degree polynomials, $k \geq 4$, according to the `face_normal_interpolation` kernel from Sec. 3.1. Gaussian quadrature on k^d points is used for both cases, necessitating use of `basis_change` in addition to the derivative kernel. Note that the face integrals of the Laplacian involve more than twice as much arithmetics as compared to the advection operator, see the second column of Table 2.

Fig. 7 presents the throughput of the combined cell and face integrals on the three hardware systems of Table 1. In order to avoid the indirect addressing associated with face integrals in general, we have considered the artificial case of periodic boundary conditions within the same cell that can directly use the vectorized data storage according to Fig. 2. The results in Fig. 7 confirm the performance results from the cell integrals in the previous figures, with up to 620 GFLOP/s on the Broadwell system and 820 GFLOP/s on KNL. Note that face integrals contribute with more than two thirds of the arithmetic work of the Laplacian for polynomial degrees up to five. For the 3D Laplacian, our code reaches a throughput of more than $3 \cdot 10^9$ degrees of freedom per second on KNL for $2 \leq p \leq 10$ and more than $2.6 \cdot 10^9$ degrees of freedom on Broadwell for $3 \leq p \leq 9$.

4 Data access patterns and MPI parallelization

In this section, we analyze the performance of the full operator evaluation including the actual data access patterns of DG cell and face integrals into the input and output vectors, as well as parallelization.

To exploit the parallelism of multi-core processors that are connected by high-speed networks in modern petascale machines, two different parallelization concepts are commonly used, the shared-memory paradigm of OpenMP/pthreads and the distributed memory concept implemented by the message passing interface (MPI). Increasingly, a mixture of both is applied to exploit intra-node and internode parallelism, respectively. MPI parallelism for finite-element based computations usually relies on domain decomposition that splits the cells among the processors. Each processor only works on its portion of the mesh. In order to exchange information on the border between subdomains, ghost elements around the locally owned subdomain are used. In our implementation, we assume one layer of ghost elements around the owned cells to be present, supported by the massively parallel algorithm from [6]. The particular form of the mesh partitioning is immaterial, as long as the information provided by the mesh infrastructure allows for a unique identification of the degrees of freedom in the locally owned cells and the ghost layer.

For shared-memory parallelism, loops over the mesh entities are split across the participating threads. Some coordination is necessary to avoid race conditions when integrals from several faces go to the same vector entries. A common scheme to avoid race conditions in many DG codes is to create a temporary storage that holds independent data for all the faces. This involves an initial loop over the cells where the face data is collected (and cell integrals are computed), a loop over the faces where only the separate face storage is referenced, and a final loop over the cells that

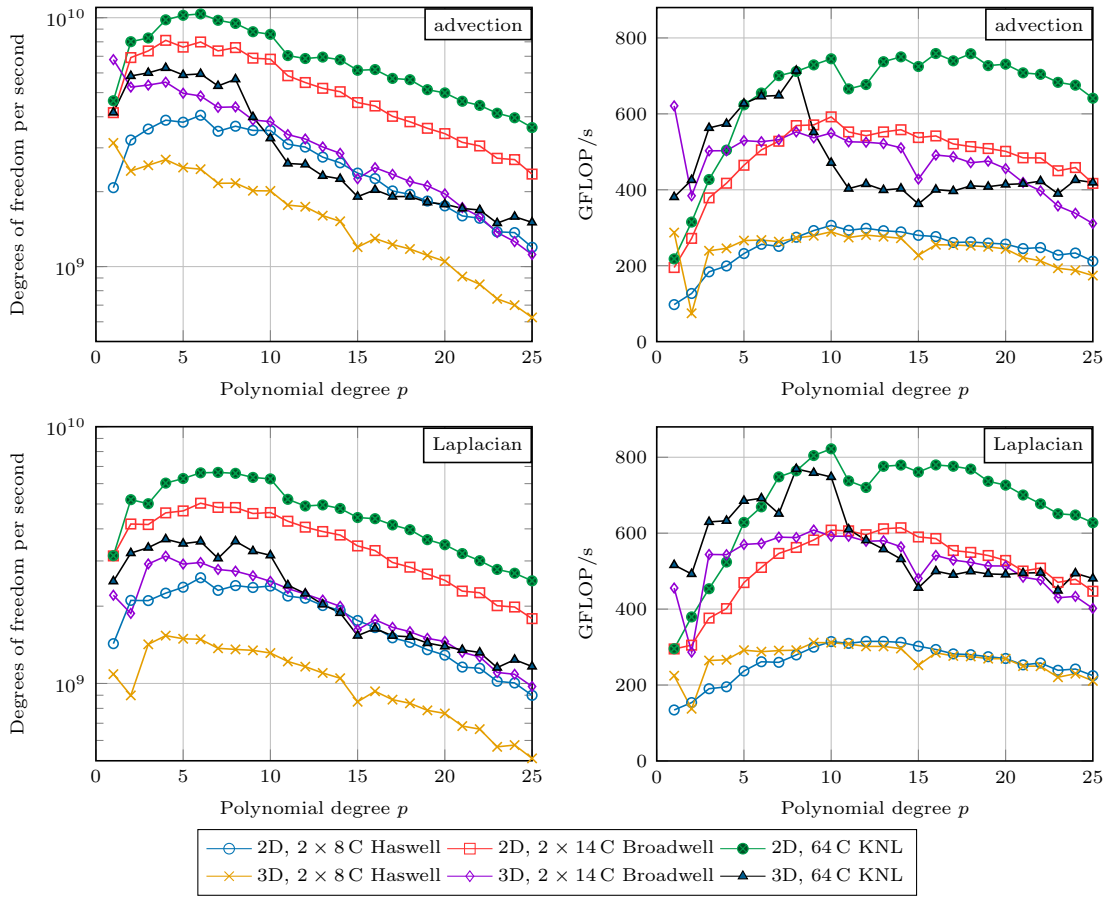


Figure 7: Throughput of cell and face kernels for advection and Laplacian in 2D and 3D without vector access on 2×8 core Intel Xeon E5-2630 v3 (Haswell), 2×14 core Intel Xeon E5-2690 v4 (Broadwell) and 64 core Intel Xeon Phi 7210 (KNL).

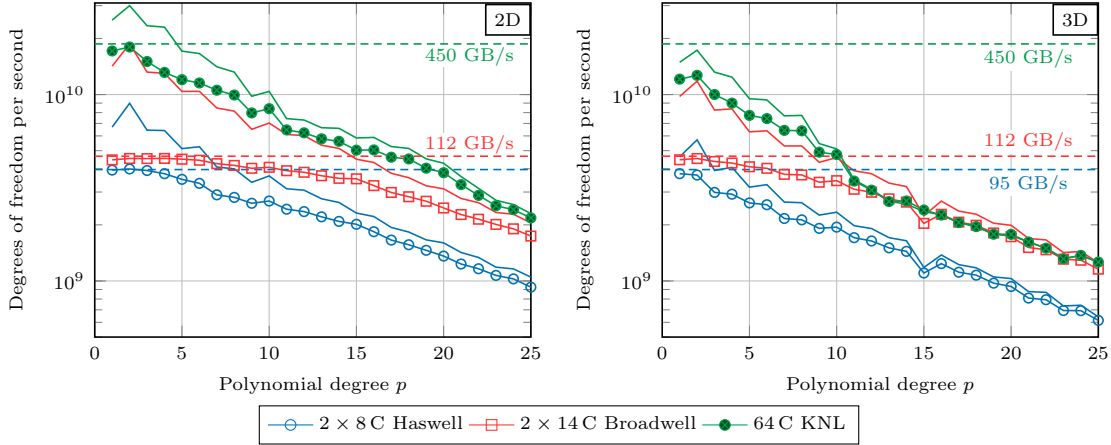


Figure 8: Verification of performance model for cell integrals of Laplacian in 2D and 3D modeling the global vector access on 2×8 core Intel Xeon E5-2630 v3 (Haswell), 2×14 core Intel Xeon E5-2690 v4 (Broadwell) and 64 core 2nd generation Intel Xeon Phi 7210 (KNL) (using hyperthreading with 128 processes). The solid lines indicate the computational throughput according to Fig. 6 and the dashed lines the memory bandwidth limit of a stream triad kernel, assuming two vector reads and one vector write.

collects the face integrals and lifts them onto the cells. The face-normal part of interpolation and integration steps of face integrals are processed in the first and third steps, whereas operations within faces are done in the face loop, see also the algorithm layout described extensively in [19]. Such a strategy involves additional data transfer since the cells are accessed twice and separate global face storage is involved. Even though it would be conceivable to keep the data storage lower with dynamic dependency-based task scheduling, the authors' experience from [31, 35] suggests that available implementations such as Intel Threading Building Blocks [46] or OpenMP tasks do typically lead to significant memory access from remote NUMA domains and other cache or prefetcher inefficiencies that lower application performance once using 10 or more cores. In this work, we therefore do not consider the various possibilities of shared-memory parallelization and analyze MPI for parallelization within the shared memory of a node.

The design pattern of using **face-separate storage** is also common in MPI-only codes, see e.g. [20], so we consider that storage scheme implemented with MPI communication in our analysis below to contrast this very common DG implementation technique against the proposed methods. To highlight the properties of separate loops for cell and face integrals, respectively, we start by an analysis of the cell integral only, which similarly translate to applying DG mass matrices or inverse mass matrices. We consider large vector sizes of around 10–50 million degrees of freedom to eliminate any cache effects.

4.1 Vector access analysis for cell integrals only

In Fig. 8, we consider the cell benchmark from Fig. 6 including the access to the global solution vectors. We assume a Cartesian geometry where our implementation simply uses the same inverse Jacobian $\mathcal{J}^{(e)}$ matrix for all the quadrature points, not accessing additional global memory. Thus, the main memory transfer in this algorithm is one vector read for the input vector, one vector write for the output vector, and one vector read operation on the output vector either because of an accumulate-into pattern or due to the read-for-ownership memory access pattern [15]. The results in Fig. 8 are contrasted against the two theoretical performance limits, the memory bandwidth limit of the vector access as measured by a STREAM triad test which give 95 GB/s, 112 GB/s, and 450 GB/s for the Haswell, Broadwell, and KNL systems, respectively, and the arithmetic throughput from the previous section. On a test similar to the one described in Fig. 4, we confirmed with the likwid tool that data transferred through the memory hierarchy has not changed except for an additional access of 24 bytes per degree of freedom that pass the solution vectors through all cache levels.

The results in Fig. 8 suggest that the memory bandwidth is the limit to throughput in 2D and at low and medium polynomial degrees $k \leq 10$, in particular for architectures with more cores such as Broadwell. On the other hand, on the Haswell and KNL systems where the memory bandwidth is higher in relation, the code is mostly compute limited in 3D, despite the high level of optimization presented above. In both cases, the envelope established by the memory throughput and the arithmetic throughput closely describes the achieved performance. The remaining gap at intermediate degrees is mostly explained by effects not captured by the simple distinction between memory bandwidth limit and arithmetic peak, but could be explained by more advanced performance models such as the execution cache memory model [15]. These experiments lead to the following design choice.

Design Choice 2 *Since cell integrals tend to be memory bound already for simple Cartesian meshes, face integrals must be interleaved with cell integrals in Algorithm 1 to re-use vector data that resides in caches. For curved geometries that involve significantly lower FLOP/byte ratios, a reduction in memory access for vector entries improves performance also on machines with abundant memory bandwidth such as KNL with its high-bandwidth memory.*

We emphasize that the compute optimizations presented in Sec. 3 are indeed essential: the upper memory limit of two loads and one store of global vectors is at around $4.7 \cdot 10^9$ degrees of freedom per second on 28 cores of Broadwell, which is higher than the compute throughput of around $2.8 \cdot 10^9$ degrees of freedom per second for the Laplacian in 3D and only slightly below the maximal throughput of $5 \cdot 10^9$ for advection in 3D according to Fig. 7. Also, the fact that the Broadwell system tends to be memory bound (for $k < 10$) on cell integrals is a result of the high level of optimization of the compute kernels.

4.2 Vectorization layout for face integrals

In this subsection, we present data structures to organize vectorization over several faces for a finite element mesh beyond the compute kernels presented in Section 3. Face integrals contain some unavoidable dispatch code that is invoked at run time, namely the selection of different data access routines depending on the local face number with respect to the cell as well as some shuffling of the data interpolated to quadrature points for 3D meshes where some faces are not in the standard orientation with respect to the cell’s local coordinate system [2]. Since face integration kernels are relatively small, the dispatch overhead reduces in importance if it is around a batch of faces with the exact same code path. The demands of integration kernels from Sec. 3.1 are satisfied by the following two design choices.

Design Choice 3 *In order to restrict vector access to only those entries where S_f and D_f from Eq. (7) are non-zero, access to the solution vector must know the highest order derivative in the evaluation routines to only read or write the necessary vector data alongside with the basis type such as `nodal_on_faces` or `hermite_like_basis`.*

Design Choice 4 *In order to simplify implementation and re-use 2D kernels, the local coordinate system on faces is always set such that reference cell gradients touch the $d - 1$ tangential directions first and the face-normal direction comes last by adjusting the order of components in the geometry tensors rather than changing indices of evaluators, see Eq. (7).*

Data Structure 1 lists a slim way of storing a pair of faces in case of vectorization. In our C++ implementation, the width of the SIMD array is set by a template argument, allowing to distinguish the SIMD width of single precision `float` and double-precision `double` or between different computer systems. The identification of the faces in a setup stage runs through an arbitrary quadrilateral or hexahedral mesh and first creates a separate `FaceInfo` object for each face. In a second step, it looks for faces with the same structure: a comparator checks for the values of `interior_face_number`, `exterior_face_number`, `subface_index`, and `face_orientations` and allows merging the faces into the same batch if they are all equal. Remarks 2 and 3 show possibilities to relax this requirement for increasing the utilization of the SIMD lanes for small problem sizes.

Remark 2 *Faces of different `subface_index`, e.g. faces with hanging nodes and others without, can be combined into the same SIMD array for small problem sizes if the interpolation matrices*

DATA STRUCTURE 1: struct FaceInfo<SIMD_WIDTH>: Face data structure with vectorization

- **unsigned int interior_cell_numbers[SIMD_WIDTH]**: Short array of indices to the cells flagged as e^- (interior); holds invalid value $2^{32} - 1$ if SIMD array not completely filled
 - **unsigned int exterior_cell_numbers[SIMD_WIDTH]**: Short array of indices to the exterior cells e^+ ; holds invalid value $2^{32} - 1$ if face at boundary or SIMD array not completely filled
 - **unsigned char interior_face_number**: local face number $l_f^- \in [0, \dots, 2d)$ within cell e^-
 - **unsigned char exterior_face_number**: local face number $l_f^+ \in [0, \dots, 2d)$ within cell e^+ for inner faces; for boundary faces, this storage location is used for storing a boundary id to distinguish between various types of boundaries in user code (e.g. Dirichlet or Neumann)
 - **unsigned char subface_index**: local subface index in $[0, 2^{d-1})$ of the exterior side of the face in case of adaptivity (2 : 1 mesh ratio required), a number of $2^8 - 1$ indicates a uniform face
 - **unsigned char face_orientations**: Index of face orientation in $[0, 8)$ for non-standard orientation on $-$ side and $[8, 16)$ on $+$ side
-

are created e.g. by selection masks into the respective interpolation array (`vblend*` instructions on `x86-64 SIMD`).

Remark 3 For special face interpolation types `nodal_at_face` or `hermite_type_basis` in the `face_normal_interpolation` of Sec. 3.1, gather access can be generalized to allow for combining partially filled SIMD lanes of different values of `interior_face_number` and `exterior_face_number`. However, this increases the amount of indirect addressing and is not considered in this work. For this scheme, Design Choice 4 is a prerequisite to keep the geometry application vectorized without further cross-lane permutations.

4.3 Numbering of degrees of freedom and vector access

In DG, all degrees of freedom of a cell can be identified by a single index because there are no hard continuity constraints linking the indices to the ones on neighboring cells. Nonetheless, the details of index storage are important for reaching high throughput. Data structure 2 details how to realize an efficient scheme in a generic finite element code. In Section 3, we have proposed an interleaved numbering of the degrees of freedom for n_{lanes} cells according to Fig. 2 as the main option. Thus, explicit vector read operations and data permutations can be skipped in favor of passing a pointer to vector data, e.g. `_m256d`, to the sum factorization kernels for cell integrals. However, the access for the cell data for face integrals must handle several different cases. As an example, consider the advection equation (1) on the degrees of freedom laid out in Fig. 2. Let us assume we work on the faces $f_1 = e_1 \cap e_2$, $f_2 = e_2 \cap e_5$, $f_3 = e_3 \cap e_4$, $f_4 = e_4 \cap e_6$, where we have

$$\text{FaceInfo}<4> = \left\{ \begin{array}{ll} \text{interior_cell_numbers} & \{1, 2, 3, 4\} \\ \text{exterior_cell_numbers} & \{2, 5, 4, 7\} \\ \text{interior_face_number} & 1 \\ \text{exterior_face_number} & 0 \\ \text{subface_index} & 255 \\ \text{face_orientation} & 0 \end{array} \right\},$$

assuming that local face numbers are 0 for the left face of a cell and 1 for the right face of a cell. In this case, the interior cell numbers e^- of the faces coincide with the interleaved numbering of the cell, allowing direct packed access. Hence, the face is identified as `IndexStorageVariants::interleaved_contiguous` for the interior side e^- . For the cell data related to the exterior side e^+ , however, the index numbering is not contiguous, as the indices to be accessed are $\{1, 64, 3, 66, \dots\}$. Thus, for the `IndexStorageVariants::interleaved_contiguous_strided` format a gather/scatter operation is needed to access the vector entries. When passing from the first four to the next four indices, a constant stride of 4 (SIMD width) appears so only the base address of the gather operation needs to be recomputed.

Data structure 2 lists `IndexStorageVariants::interleaved_contiguous_mixed_strides` as a third interleaved case. This case appears on ghosted cells of a processor with rank p_j which only holds some of the cells to which the owning processor with rank p_i has assigned interleaved storage. This scenario can in general not be avoided if only a single layer of ghost elements is

DATA STRUCTURE 2: class DoFInfo: Storage scheme for indices to degrees of freedom

- `enum class IndexStorageVariants`: list of identifiers for different face storage types.
 - `contiguous`: Contiguous degrees of freedom in each cell separately, storing only the start index. Read from `dof_indices_contiguous`.
 - `interleaved_contiguous`: Contiguous degree of freedom numbering within cells that is additionally interleaved over the SIMD arrays with unit stride, allowing for direct packed array access from the `SIMD_WIDTH`-th index in `dof_indices_contiguous`.
 - `interleaved_contiguous_strided`: Interleaved and contiguous storage within the cells. It has a fixed stride of `SIMD_WIDTH` from one degree of freedom to the next, but a variable stride from one SIMD lane to the next.
 - `interleaved_contiguous_mixed_strides`: As opposed to `interleaved_contiguous_strided`, this storage scheme has a separate stride from one degree of freedom to next within the SIMD arrays. The strides are accessed from the vector `dof_indices_interleaved_strides`.
 - `full`: For handling continuous elements, generic storage with a separate index for each degree of freedom on each element is needed. Read from `dof_indices`.
- `std::vector<unsigned int> dof_indices`: Generic index storage for generic elements, size equal to $n_{\text{cells}}k^d$, possibly including constraint information [34].

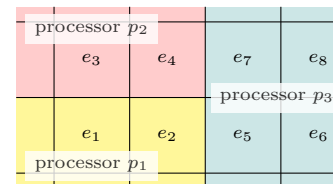
The following four fields keep three vectors that allow integrators on interior faces (indexed by 0), exterior faces (indexed by 1), and on cells (indexed by 2) to directly access the appropriate location in the solution vectors without going over `FaceInfo`.

- `std::vector<IndexStorageVariants> index_storage_variant[3]`: Three vectors that define the detected index storage variant.
 - `std::vector<unsigned int> dof_indices_contiguous[3]`: Three vectors storing the first index in a contiguous storage scheme from types `IndexStorageVariants::contiguous` through `IndexStorageVariants::interleaved_contiguous_mixed_strides`.
 - `std::vector<unsigned int> dof_indices_interleave_strides[3]`: Three vectors storing the stride for each SIMD lane between consecutive degrees of freedom for `IndexStorageVariants::interleaved_contiguous_mixed_strides`.
 - `std::vector<unsigned char> n_simd_lanes_filled[3]`: The number of SIMD lanes that are actually representing real data. For all lanes beyond the given number the vectorized integration kernels carry dummy data without read or write reference into vectors.
-

present around the locally owned subdomain of each MPI rank according to the algorithm [6]. As an example, consider the case of `SIMD_WIDTH=2` for a cell at the corner with two additional ranks according to Fig. 9. Further, assume that the face $e_2 \cap e_4$ is processed by processor p_2 and face $e_2 \cap e_5$ by p_3 , respectively. If the indices on p_1 are interleaved between e_1 and e_2 , this interleaved access is also possible on p_2 . However, p_3 has no knowledge of e_1 , so the ghost indices transformed to the MPI-local index space on p_3 appear to have stride 1 for e_2 . The `interleaved_contiguous_mixed_strides` path is also used for storing the case of partially filled SIMD lanes.

Data Structure 2 proposes to store the indices of the degrees of freedom as 32-bit unsigned integer numbers. We note that the index storage refers to MPI-local numbering that starts with the locally owned range from zero. Moreover, we use a global enumeration of degrees of freedom where 64-bit unsigned integers are possible for solving problems that have more than 4 billion unknowns—but at no more than 4 billion unknowns per MPI process.

In Data Structure 2, we choose to redundantly store the start indices of the cells on both sides of interior faces, additionally to the start indices for cells. The indices on faces could also be deduced from the stored cell indices and the face numbers in `FaceInfo`. Since they only represent between 4 and 13 bytes for each side of a face, it is usually more efficient to load this information from a precomputed array than to recompute the face’s index storage variant and start index during the operator evaluation.



4.4 Partitioning of face integrals with MPI parallelization

The arithmetic work and memory access of face integrals is minimized if testing from both sides of a face is done simultaneously, using the unique numerical flux for both sides and possible terms from integration by parts. In this scheme, vector entries stored on neighboring processors at the subdomain interfaces are needed. Assuming a balanced partitioning of cells to be given from the domain decomposition, we divide the face integrals *pairwise* on each interface $p_i \cap p_j$ of two processors p_i and p_j to reach balanced work on faces. We set the following two restrictions:

- If the set of shared faces F_{ij} along the interface between p_i and p_j contains two faces f_a and f_b referring to a single cell e from processor p_i , we schedule both integrals on p_j . This approach reduces the amount of data sent, since the data from e sent from p_i to p_j is used for two (or more) face integrals.
- If a face $f \in F_{ij}$ is on an interface of different mesh levels (hanging node) where p_i is on the coarser side and p_j on the refined side, we schedule the integral on p_j . If p_j holds all children, which is the most common case, we again reduce the data sent. Furthermore, this assumption allows to classify the off-processor side of faces as exterior cells e^+ according to `FaceInfo` in Algorithm 1 and have subface interpolation only on the exterior side, allowing for a single `subface_index` variable.

Since the number of cells is balanced and each processor gets half the faces with each of its neighbors, the faces are also globally split evenly. This algorithm is cheaper than balancing faces more globally that involves more complicated strategies. We observed experimentally that in all our setups, the number of locally computed faces does not differ by more than up to a few dozens pf faces among all MPI ranks on meshes more or less independent of the number of cells.

4.5 Index access and ghosting

For the integration kernel, remote (ghosted) data on faces at processor boundaries must be imported before the respective face integrals are issued. Furthermore, integral contributions computed on a remote processor must finally be accumulated into the owner. Following the layout described in [34], we do this by dedicated vector types that provide additional space beyond the locally owned range to fit the ghost data. Note that we only communicate those cells where the face integrals demand data, not the full ghost layer. Outside the integration kernels, such as in time steppers or linear solvers, only the vector data of the locally owned range (one-to-one map over processors) is exposed and ghosted data is ignored. Restricting the copy only to the ghosted entries is preferred because we aim for performance close to the hardware limits, where a copying of the whole vector together with the ghost entries would significantly increase computational costs.

Fig. 10 lists the throughput of the full matrix-vector product including the MPI communication. The communication of all the degrees of freedom of remote cells needed for face integrals is labeled as “full” in the figure. To ensure comparable problem sizes, we use Cartesian meshes whose size varies with the polynomial degree, namely a 128^3 mesh for degrees $p = 1, 2$, a 64^3 mesh for $3 \leq p \leq 5$, a 32^3 mesh for $6 \leq p \leq 11$, a 16^3 mesh for $12 \leq p \leq 23$, and an 8^3 mesh for $p \geq 24$. For this choice, the problem has between 8 and 57 million degrees of freedom. Fig. 10 reveals sudden drops in performance when the mesh size is reduced. At these points, the volume-to-surface ratio for the next smaller mesh level gets lower and a larger proportion of cells must be exchanged. Note that MPI communication in this experiment is in fact within a shared-memory architecture, so the cost is related to some `memcpy` kernels as well as pack and unpack routines which are memory bandwidth bound. This part consumes more than 40% of the operator evaluation time for $6 \leq p \leq 11$, and we have verified that it indeed runs at full memory speed of 110 GB/s on Broadwell.

The algorithm of sending all data of a cell can be improved by observing that the `face_normal_interpolation` kernel will only touch some of the degrees of freedom of a cell for certain bases and derivatives, namely those where S_f and possibly D_f of Eq. (7) are non-zero. In this case, only the relevant part of the cell’s vector entries must be communicated and packed/unpacked. Algorithm 3 presents the algorithmic setup. The algorithm keeps the integration and vector access routines agnostic of this fact: we provide storage for all the degrees of freedom of a cell but only populate some of the entries with data. Copying the slim indices adds another indirection to the

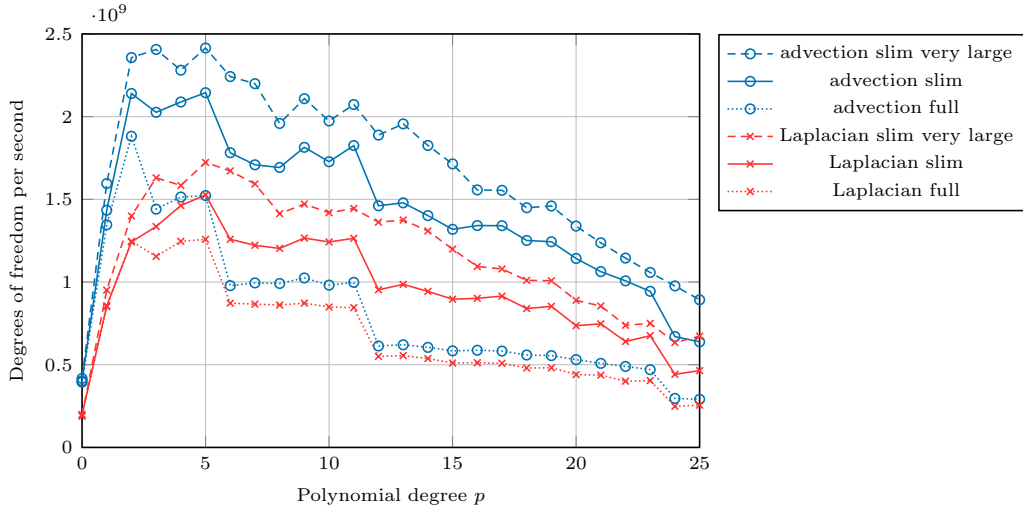


Figure 10: Influence of the MPI communication pattern on throughput as a function of the polynomial degree on 28 Broadwell cores for the Laplacian on a Hermite-like basis. The problem sizes are between 8 and 57 million DoFs and jump to the next smaller grid at $p = 3$, $p = 6$, $p = 12$, and $p = 24$, increasing the proportion of cells at processor boundaries from 4% at $p \leq 2$ to more than 80% at $p \geq 24$. The dashed and dashdotted lines display the throughput at sizes above 160 million degrees of freedom with the slim data communication.

“pack” stage of the MPI data exchange because the data to be sent is not contiguous in memory. Fortunately, the code pattern is exactly the same as the selection of some entries among the locally owned part for data transfer, so existing implementations can be readily extended. Note that Algorithm 3 cannot be directly implemented via general-purpose vector classes with MPI facilities such as PETSc [5] or Trilinos’ Epetra and Tpetra [17, 18] without deep vector copies, which is why we use our own specialized implementation inside `deal.II` that is interlinked with the needs of the integrators.

The proposed slim MPI communication leads to simpler code than an alternative concept that uses a face-separate storage scheme at processor boundaries that runs `face_normal_interpolation` before communication. A different storage scheme for data from ghosted cells with other strides would lead to a lane divergence in case not all faces in the SIMD array are adjacent to a ghosted cell: the lanes without ghosted cells would still need to perform an interpolation step whereas the ones representing ghosted cells would not.

Fig. 10 shows that the slim MPI communication of Algorithm 3 improves throughput by more than 30% for the Laplacian with $p = 6$ at 8.9 million degrees of freedom and by almost 70% for the advection operator with $p = 6$. The drops in throughput when going to smaller meshes with larger surfaces at processor boundaries are still visible for the slim implementation but much less pronounced. As a point of reference, Fig. 10 also contains data from experiments on problems on a mesh that is more than 20 times larger where the slim MPI communication amounts to less than 10% of the operator evaluation time.

In Table 3 we compare the throughput of the proposed slim MPI data exchange for the 3D Laplacian on a Hermite-type basis with a face-separate storage as used e.g. in [20, 35]. The face-separate storage breaks the face integrals into a separate loop and handles the cell–face exchange through a global data structure for faces. This setup simplifies the MPI data exchange and allows for easier threading, but at a much higher memory access since the result vector must be accessed in two separate loops and the face storage in three loops [35]. For face-separate storage a basis with collocation of nodal points and quadrature points is more advantageous because it can skip the `basis_change` algorithm in cell integrals. The results highlight that the proposed method with a single loop for cell and face integrals is almost twice as fast for degree $p = 5$ and still 25% faster for $p = 11$. The face-separate storage only becomes superior at $p > 15$ where the advantages of collocated node and quadrature points get significant. Note that the face-separate storage scheme runs at full memory throughput with > 90 GB/s for all degrees up to $p = 11$, whereas the proposed

ALGORITHM 3: Slim MPI communication

- Required input:
 - Precomputed type of basis: nodal at boundary, Hermite-type, generic.
 - Which terms are required for inner face integrals (only cell terms, values on face, values and first derivatives on face)?
- `update_ghost_values` fills the ghosted data, `compress` accumulates integral contributions to the respective entries at the owner. The communication is established according to the following three options:
 - If no face integrals, do nothing in DG (or cell-only ghost exchange of continuous elements).
 - If only face values and basis nodal at boundary, send only one single layer of k^{d-1} degrees of freedom per cell at the interface.
 - If only up to first derivatives on face and Hermite-type basis, send only the two layers representing values and normal derivatives with $2k^{d-1}$ degrees of freedom per cell at the interface.

We provide storage for all degrees of freedom of the ghosted cell in the vector but only fill the entries where the interpolation matrices S_f and D_f are nonzero (avoids separate code paths).

Table 3: Throughput and measured memory throughput for evaluation of the 3D Laplacian on 2×14 Broadwell cores with the proposed implementation on a Hermite-like basis against scheme with separate face storage on a with collocated nodal and quadrature points that minimizes arithmetic operations.

polynomial degree p	2	3	5	8	11	15	20
	million degrees of freedom per second, MDoF/s						
proposed scheme	1243	1336	1527	1203	1264	896	736
face-separate storage	551	646	897	1014	1077	901	912
	measured memory throughput, GB/s						
proposed scheme	62.2	68.6	74.0	71.1	64.4	61.1	63.6
face-separate storage	106	106	107	102	90.7	75.1	72.6

scheme does not utilize the full RAM bandwidth, despite being substantially faster. Thus, even an idealized version of the face-separate storage would be necessarily slower than our proposed implementation.

Fig. 11 specifies the cost of the various algorithmic components of the DG operator evaluation. Timings are based on the RDTSC timer register of Intel processors that have small enough overhead to be placed in inner loops. When compared to the compute-only part from Fig. 7, we observe a drop in performance by approximately a factor of 2 for the Laplacian for $2 \leq p \leq 10$. Clearly, the MPI communication (including `mempcpy` and `pack/unpack`) takes a significant share of time for the smaller computation. Sum factorization on cells which is of complexity $\mathcal{O}(p)$ in the number of degrees of freedom gets more expensive for higher degrees, but it takes less than 50% of the evaluation time for all degrees $p \leq 10$. To show uncertainties and influence of timers on out-of-order execution that are significant at $p < 4$, we also include reference runs with disabled timers, displayed by diamonds.

Remark 4 *Note that the above experiments are performed in shared memory, so the MPI data exchange boils down to some form of `mempcpy` operations in the MPI implementation besides the `pack/unpack` parts. Thus, there is no direct advantage of overlapping the communications with computations and the transfer cost does show up in our profiles, as opposed to communication over an Infiniband-like fabric that indeed is overlapped with our implementation.*

4.6 Performance on Haswell, Broadwell and Knights Landing

Fig. 12 shows our main result, the performance of the presented implementation on the DG discretization of the advection equation (1) and the DG discretization of the Laplacian (2), including the full code with MPI data exchange. We compare the actually achieved performance (lines with marks) to the theoretical arithmetic performance limit established in Fig. 7 and the memory

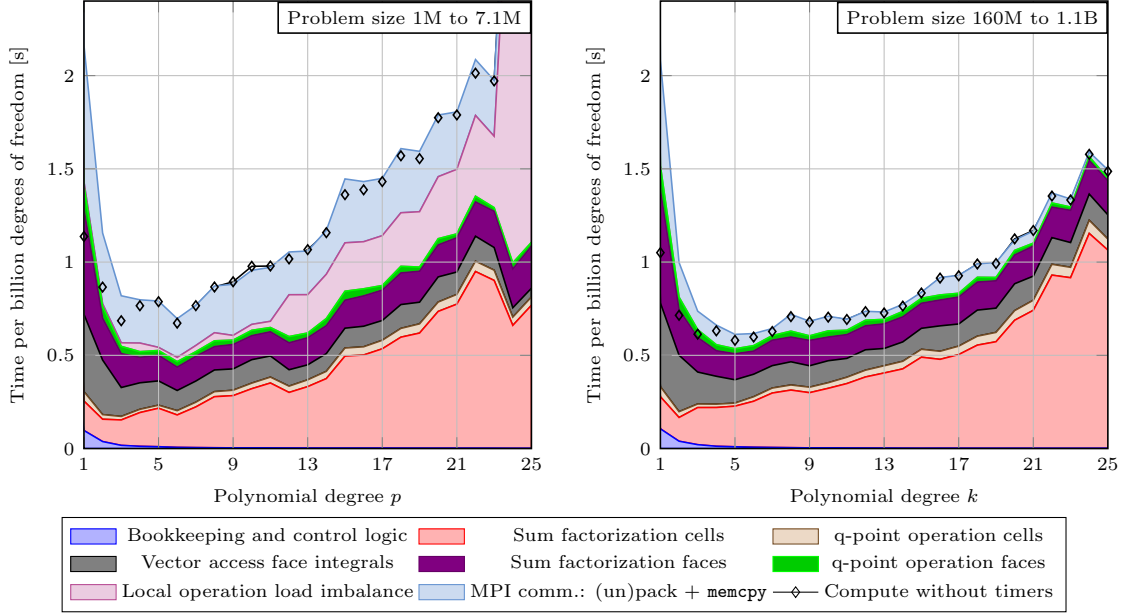


Figure 11: Breakdown of computation times on different phases for the 3D Laplacian for a small sized experiment at 1–7.1 million DoFs and a large experiment at 160 million to 1.1 billion DoFs. The timings have been recorded on 2×14 Broadwell cores and rescaled to the time for a fixed fictive size of 1 billion (10^9) degrees of freedom.

bandwidth limit. The actual throughput is between $0.41\times$ and $0.77\times$ the arithmetic throughput numbers for the 2D advection operator at $2 \leq p \leq 15$ for all three architectures and mostly around $0.55\times$. For the 2D Laplacian, typical values are at $0.69\times$ of the theoretical throughput on Haswell, $0.63\times$ on Broadwell, and $0.55\times$ on KNL. In analogy to Fig. 11, the gap in performance can be accounted to the MPI communication (around 5–8% of operator evaluation in 2D), the gather access pattern at half the faces (around 15% of operator evaluation time)³ and, for degrees less than 3, to overhead in accessing the storage data structures such as Data Structure 2. If we take into account these factors, performance is within 10% of the possible roofline on Haswell and Broadwell and within 20% on KNL. In the likwid analysis, the remaining performance penalties were mostly identified to be memory stalls due to wait for L2/L3 caches or memory from imperfect prefetching. To account for these effects, a more detailed look at the memory hierarchy would be necessary beyond the roofline concepts applied here, such as the execution cache memory performance model [15].

In three space dimensions, we observe a considerably larger gap between the model and the actual performance. On Haswell, we record a throughput of $0.56\times$ and $0.63\times$ the value for the compute-only case for $2 \leq k \leq 10$ for advection and the Laplacian, respectively, the numbers for Broadwell are $0.41\times$ and $0.49\times$, and for KNL we recorded $0.39\times$ in both cases. As documented by Fig. 11, up to a third of the compute time is consumed in the MPI communication and pack/unpack already for p between 6 and 11. If subtracting the data exchange, the Laplacian reaches around 1.8 to 2.1 billion degrees of freedom per second on 28 Broadwell cores and 64 KNL cores for $4 \leq k \leq 9$, i.e., more than 70% of the compute performance of Fig. 11. Besides the cost for gather and scatter operations, the performance gap not further quantified and attributable to memory stalls is around 20% in 3D.

The algorithms are equally beneficial for large-scale parallel simulations as shown in Table 4. We record almost ideal strong scaling until around 0.7 ms and reasonable scaling down to 0.3 ms. The main reason for the loss in efficiency above 0.7 ms is the larger proportion of pack/unpack and `memcpy` routines in the communication reported in Fig. 11. The proposed algorithms have delivered excellent performance to even larger scale up to almost 10,000 nodes (147,456 cores) in

³The gather operation occurs on slightly more than half of the faces: in the computations shown in Fig. 11 around 45...50% of the faces involve direct array access according to `interleaved_contiguous` type, 40...50% involve the `interleaved_contiguous_strided` variant, and the remainder 10% have mixed strides.

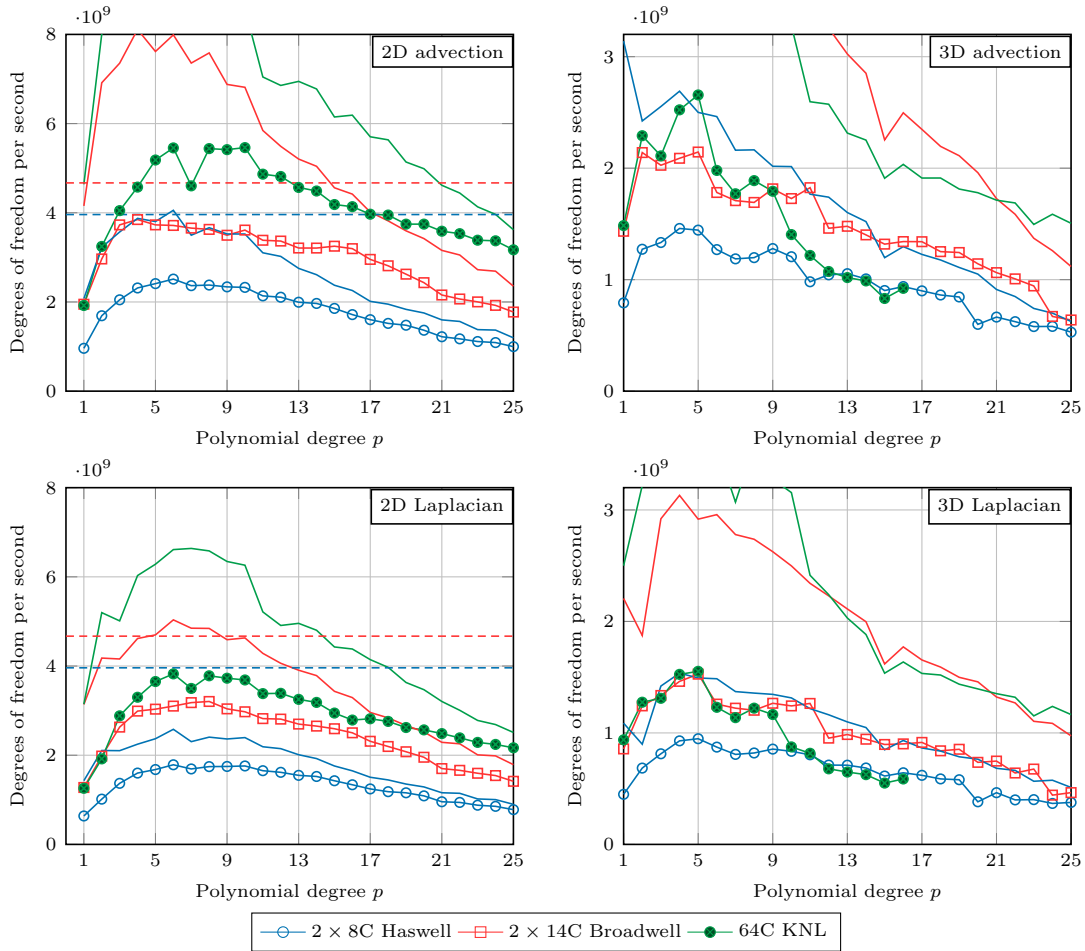


Figure 12: Comparison of the throughput on the 2D and 3D advection operator and Laplacian on Haswell, Broadwell and KNL. The measurements are compared to the theoretical throughput of the kernels from Fig. 7 (solid lines of respective color) and the memory bandwidth of 95 GB/s on Haswell, 112 GB/s on Broadwell (dashed lines) and 450 GB/s on KNL (outside shown range) for the idealized setting of two vector reads and one vector write.

Table 4: Strong scaling of experiment on 3D Cartesian mesh with 262,144 cells and $p = 5$ (56.6 million degrees of freedom) on Xeon E5-2697 v3 (2×14 cores at 2.6 GHz) based cluster on up to 512 nodes with 14,336 cores. Numbers are reported as the absolute run time in milliseconds [ms] of a matrix-vector product including communication and in terms of throughput measured as million degrees of freedom per second and core (MDoF/s/core) reporting the parallel efficiency.

# nodes	1	2	4	8	16	32	64	128	256	512
double precision										
time [ms]	41.6	21.4	11.7	6.23	3.12	1.43	0.798	0.495	0.409	0.236
MDoF/s/core	48.7	47.2	43.3	40.6	41.6	44.1	39.6	31.9	19.3	16.8
single precision										
time [ms]	21.9	11.8	6.12	3.07	1.48	0.814	0.494	0.324	0.285	0.177
MDoF/s/core	92.4	86.0	82.6	82.3	85.1	77.6	64.0	48.7	27.7	23.3

[37, 32].

5 Representation of geometry

In Algorithm 1, we assumed the inverse Jacobian $\mathcal{J}^{(e)}$ of the transformation from unit to real cell to be given. The computation of integrals also involves the determinant of the Jacobian and normal vectors \mathbf{n} derived from the Jacobian. The Jacobian is often defined as the derivative of a piecewise m -th degree polynomial description of the geometry through some points which we refer to as mapping support points $\mathbf{x}_{\text{msp}}^{(i)}$, $i = 1, \dots, n_{\text{points}}$, but it can also be defined by analytical tangent vectors on the geometry [3]. Extending over a short discussion in [34], a high-performance implementation for arbitrary geometries can select between at least four main variants:

- (G1) Storage of mapping support point locations $\mathbf{x}_{\text{msp}}^{(i)}$ for all indices i in the mesh with usual indirect addressing of continuous finite elements and subsequent tensor product evaluation. This involves transfer of *somewhat less than 3 double precision values* per quadrature point for isoparametric mappings, depending on the polynomial degree which determines the weight on the higher valence entities, i.e., mesh vertices, edges, and faces.
- (G2) Storage of all quadrature points $\mathbf{x}_{\text{qp}}^{(q)}$ in physical space, from which the Jacobian can be computed by a collocation derivative. This needs *3 double precision values* per quadrature point in 3D. For face integrals, separate data is needed except for Gauss-Lobatto like integration rules.
- (G3) Pre-computation of $\mathcal{J}^{(e)}$ in all quadrature points of the mesh; for face integrals, separate data is needed. Storing the inverse Jacobian and the determinant of the Jacobian involves transfer of *10 double precision values* per quadrature point in 3D.
- (G4) Pre-computation of the effective coefficient in the particular equation at hand, e.g. a symmetric $d \times d$ tensor $(\mathcal{J}^{(e)})^{-1} (\mathcal{J}^{(e)})^{-\text{T}} \det(\mathcal{J}^{(e)})$ for the cell term of the Laplacian (*6 double precision values* in 3D) or the vector $(\mathcal{J}^{(e)})^{-1} \mathbf{c}(\mathbf{x}) \det(\mathcal{J}^{(e)})$ for the advection equation (*3 double precision values* in 3D), a technique used e.g. in Nek5000 [14].

Furthermore, coefficients such as $\mathbf{c}(\hat{\mathbf{x}}^{(e)}(\boldsymbol{\xi}))$ in Algorithm (1) can be pre-computed and loaded during the operator evaluation or computed on the fly based on the location of the quadrature point $\mathbf{x}_{\text{qp}}^{(q)}$. The pre-computed variants can also be combined with simple memory compressions, such as the constant-Jacobian case on affine meshes [34] or constant-in-one-direction case on extruded meshes. The results in the previous section have shown that the operator evaluation is usually compute bound on Cartesian meshes, in particular on the Haswell and KNL systems. Since the first two options (G1) and (G2) involve additional computations, it is not clear a priori whether to prefer tabulation with its higher memory transfer or rather computation on the fly.

For a generic software package, a further factor that must be taken into account are possible computations or memory access in user code. Our experience is that these tend to rather introduce compute-bound patterns including table lookups, branches, or computations, such that we prefer

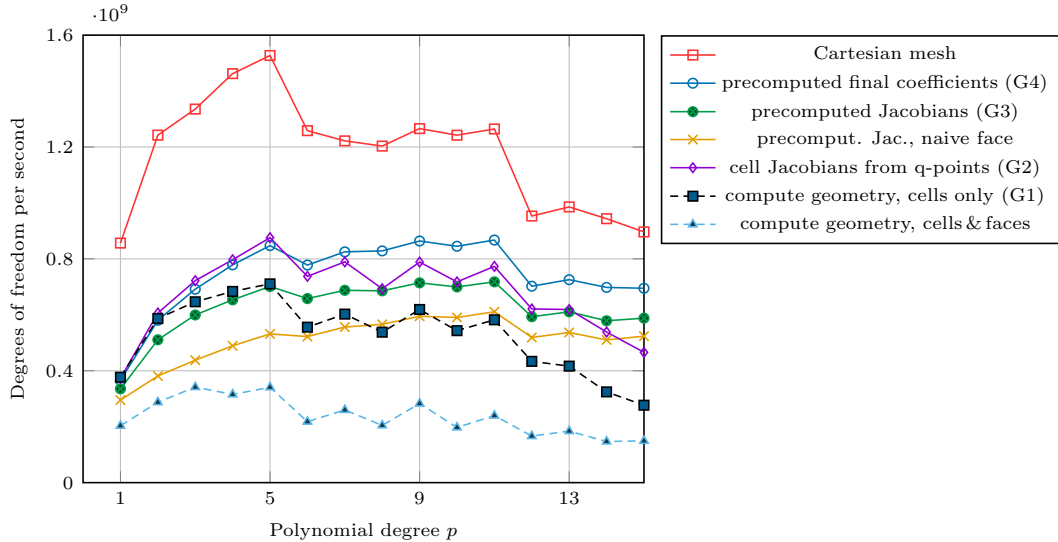


Figure 13: Throughput of 3D Laplacian kernel for various ways to represent a curved geometry on 28 cores of Broadwell.

the pre-computed variants. In `deal.II`, we use a sparse-matrix-like storage scheme that allows different cells and faces to hold arrays of different lengths, for example to flexibly switch between Cartesian meshes or fully curved meshes or hp-adaptive data structures. We propose to keep different arrays for quantities such as normal vectors, Jacobians, and Jacobian determinants, so that only the data that is actually needed for a particular operator evaluation is loaded from memory. We observed that attempts to interleave storage of different quantities closer together has a negative impact on performance because data may overlap in cache lines or hardware prefetchers would eagerly load unnecessary data.

The variants (G3) and (G4) result in different code layouts, respectively: (G3) allows for the definition of arbitrary weak forms and integration of nonlinear terms in general scenarios by separate control over the operators on trial functions and test functions (e.g. `get_value`, `get_gradient`, or `test_by_gradient`). The variant (G4) hardcodes the differential operator in the coefficient. Certain operators like the Laplacian or advection are treated more efficiently with the latter approach. To satisfy these opposing demands, we allow for both in our generic implementation.

Fig. 13 shows the throughput of the 3D Laplacian with the various geometry representations listed above on a hypershell mesh and high-order polynomial geometry descriptions. The problem size is similar to Cartesian meshes with 8 million to 57 million degrees of freedom. As can be seen from the performance model in Fig. 14, the reason for the gap to the Cartesian mesh case is that the code is clearly memory bandwidth bound in the variable geometry case. The pre-computed geometry options show the most consistent performance, despite the highest memory transfer as an inverse Jacobian and the Jacobian determinant (G3) or final coefficients of (G4) must be loaded for each quadrature point. A distinctive trend is that the memory bandwidth limit renders throughput measured as the number of degrees of freedom processed per second almost constant for a wide range of polynomial degrees, $3 \leq p \leq 11$, since the data accessed per degree of freedom is $\mathcal{O}(1)$.

When computing the full geometry of both cells and faces from a continuous FE space, marked “compute geometry, cells & faces” in Fig. 13, performance does not exceed 350 million degrees of freedom per second. Since face integrals only access k^{d-1} data points out of the k^d elemental degrees of freedom, it is preferable to at least store the evaluated geometry of the faces as in (G1). Another alternative is provided by the item “precomputed Jacobian, naive face” where we first compute the full gradient $(\mathcal{J}^{(e)})^{-T} \nabla_{\xi} u$ and then multiply by \mathbf{n} . All variants (G1)–(G4) in Fig. 13 get the normal gradient $\mathbf{n} \cdot \nabla_{\mathbf{x}} u$ on faces by computing $\mathbf{j}_{\mathbf{n}} \nabla_{\xi}$ accessing the normal times the Jacobian $\mathbf{j}_{\mathbf{n}} = \mathbf{n} \cdot (\mathcal{J}^{(e)})^{-T}$ according to Design Choice 5.

Design Choice 5 For discretizations involving the gradient on faces such as the symmetric interior penalty DG discretization of the Laplacian (2) where the inverse Jacobian $(\mathcal{J}^{(e)})^{-T}$ and the

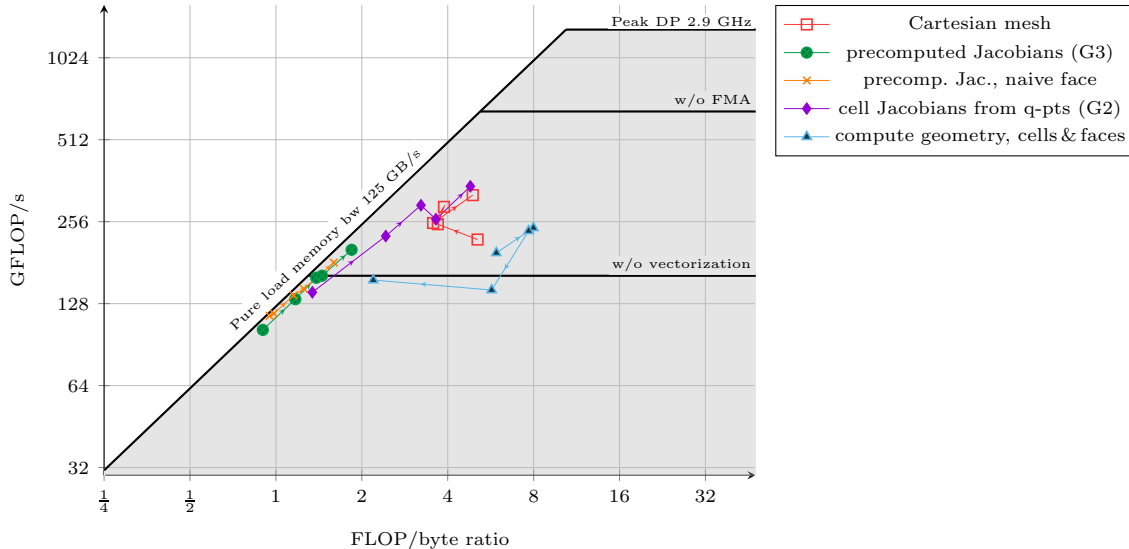


Figure 14: Roofline model for the evaluation of the 3D Laplacian with different geometry variants on 2×14 cores of Broadwell, displaying the data for $p = 1, 3, 5, 8, 11$ for five cases from Fig. 13 regarding the geometry representation. Higher degrees are located further to the right, except for the computation of the full geometry where tensor product kernels at $p = 11$ spill to main memory at a FLOP/byte ratio of 2.2. The arithmetic balance is based on measured memory throughput and measured GFLOP/s rates with the likwid tool. Arrows indicate increasing polynomial degrees.

normal vector \mathbf{n} appear together, it is advisable to use access functions of the type `get_normal_times_gradient` that can directly access a pre-stored vector $\mathbf{j}_n = \mathbf{n} \cdot (\mathcal{J}^{(e)})^{-T}$ (normal times inverse Jacobian). This approach reduces the memory access from $2d^2 + d$ doubles per quadrature point to $2d$ doubles for an interior face.

With respect to the cell integrals, we see that geometry computation from a continuous finite element field (G1) that involves gather functions is only competitive for low degrees where the reduced memory access pays off. For $p > 5$, some pre-computation is indeed preferable. The computation of cell Jacobians from the pre-computed positions of the quadrature points that only invokes `collocation_derivative` is a very attractive option and even outperforms the pre-computed final coefficients option for low degrees. However, for large degrees $p > 10$ the computations of derivatives through the collocation approach involves temporary data arrays that go to outer level caches and eventually spill to main memory.

Fig. 14 displays the measured performance of operator evaluation in terms of the roofline performance model [48]. The pre-computed versions are essentially at the limit of the memory bandwidth. For the collocation derivative approach that gets the Jacobian from the quadrature point locations, a considerably higher arithmetic intensity with some components dominated by memory transfer and others being compute-bound is observed, in particular at higher degrees. Note that inverting the Jacobian involves about three times as many multiplications as FMAs. The Cartesian mesh case is, as discussed in the previous sections, a bit away from the theoretical performance limits, which is mostly due to the MPI data exchange that consumes almost one third of the time at full memory bandwidth limit.

6 Conclusions and future developments

We have presented a detailed performance analysis of matrix-free operator evaluation for discontinuous Galerkin methods with cell and face integrals. The methods are specialized for quadrilateral and hexahedral meshes and use sum factorization techniques for computing the integrals by quadrature. The implementations are available to both explicit time integration as well as for the solution of linear and nonlinear systems with iterative solvers that spend the bulk of their time

in matrix-vector products or residual evaluations. This work has highlighted the most important algorithmic choices to reach optimal performance. We have presented efficient sum factorization kernels with various compute optimizations that make use of explicit vectorization over several cells and apply an even-odd decomposition for further reduction of the arithmetics of the local 1D interpolation. The resulting local kernels have been shown to reach up to 60% of arithmetic peak on Intel Haswell and Broadwell processors and up to 50% of peak on an Intel Knights Landing manycore system. For complex geometries, we found that storing the geometry data on the faces delivers much better throughput than computation on the fly, whereas computing the inverse Jacobian for the cell integral from the quadrature point locations by a collocated derivative algorithm can improve performance over loading precomputed Jacobians from main memory.

Our experiments show that the proposed highly optimized local kernels render cell integrals alone mostly memory bandwidth bound for low and moderate polynomial degrees up to ten. Thus, cell and face integrals must be interleaved for reaching optimal performance. When it comes to the MPI parallelization, our experiments have identified the MPI data exchange operations to take up to a third of the operator evaluation time on a single node, reducing the throughput from around 2 billion degrees of freedom on 28 Broadwell cores (at up to 430 GFLOP/s) to around 1.5 billion degrees of freedom per second (at up to 320 GFLOP/s), even after optimizing the MPI data transfer for special polynomial bases. Thus, a future goal is the development of efficient shared-memory parallelization schemes or MPI shared memory schemes according to the MPI-3 standard. Furthermore, these alternative parallelization concepts reduce the amount of duplicated data in general, promising better use of many-core architectures that have less memory per core available than today's multi-core processors.

References

- [1] D. S. ABDI, L. C. WILCOX, T. C. WARBURTON, AND F. X. GIRALDO, *A GPU-accelerated continuous and discontinuous Galerkin non-hydrostatic atmospheric model*, The International Journal of High Performance Computing Applications, (2017), in press, doi:10.1177/1094342017694427.
- [2] R. AGELEK, M. ANDERSON, W. BANGERTH, AND W. L. BARTH, *On orienting edges of unstructured two- and three-dimensional meshes*, ACM Transactions on Mathematical Software, 44 (2017), pp. 5:1–5:22, doi:10.1145/3061708.
- [3] D. ARNDT, W. BANGERTH, D. DAVYDOV, T. HEISTER, L. HELTAI, M. KRONBICHLER, M. MAIER, J.-P. PELTERET, B. TURCK SIN, AND D. WELLS, *The deal.II library, version 8.5*, Journal of Numerical Mathematics, 25 (2017), pp. 137–145, doi:10.1515/jnma-2017-0058, www.dealii.org.
- [4] D. ARNOLD, F. BREZZI, B. COCKBURN, AND L. D. MARINI, *Unified analysis of discontinuous Galerkin methods for elliptic problems*, SIAM Journal on Numerical Analysis, 39 (2002), pp. 1749–1779, doi:10.1137/S0036142901384162.
- [5] S. BALAY, S. ABHYANKAR, M. F. ADAMS, J. BROWN, P. BRUNE, K. BUSCHELMAN, L. DALCIN, V. ELJKHOUT, W. D. GROPP, D. KAUSHIK, M. G. KNEPLEY, L. C. MCINNES, K. RUPP, B. F. SMITH, S. ZAMPINI, H. ZHANG, AND H. ZHANG, *PETSc users manual*, Tech. Report ANL-95/11 - Revision 3.7, Argonne National Laboratory, 2016. <http://www.mcs.anl.gov/petsc>.
- [6] W. BANGERTH, C. BURSTEDDE, T. HEISTER, AND M. KRONBICHLER, *Algorithms and data structures for massively parallel generic finite element codes*, ACM Trans. Math. Softw., 38 (2011), pp. 14:1–14:28.
- [7] P. BASTIAN, C. ENGWER, J. FAHLKE, M. GEVELER, D. GÖDDEKE, O. ILIEV, O. IPPISCH, R. MILK, J. MOHRING, S. MÜTHING, M. OHLBERGER, D. RIBBROCK, AND S. TUREK, *Hardware-based efficiency advances in the EXA-DUNE project*, in Software for Exascale Computing – SPPEXA 2013-2015, H.-J. Bungartz, P. Neumann, and W. E. Nagel, eds., Springer, Cham, 2016, pp. 3–23, doi:10.1007/978-3-319-40528-5_1.
- [8] P. BASTIAN, C. ENGWER, D. GÖDDEKE, O. ILIEV, O. IPPISCH, M. OHLBERGER, S. TUREK, J. FAHLKE, S. KAULMANN, S. MÜTHING, AND D. RIBBROCK, *EXA-DUNE: Flexible PDE solvers, numerical methods and applications*, in Euro-Par 2014: Parallel Processing Workshops, vol. 8806 of Lecture Notes in Computer Science, Springer, 2014, pp. 530–541.
- [9] J. BROWN, *Efficient nonlinear solvers for nodal high-order finite elements in 3D*, J. Sci. Comput., 45 (2010), pp. 48–63.
- [10] C. D. CANTWELL, D. MOXEY, A. COMERFORD, A. BOLIS, G. ROCCO, G. MENGALDO, D. DE GRAZIA, S. YAKOVLEV, J.-E. LOMBARD, D. EKELSCHOT, B. JORDI, H. XU, Y. MOHAMIED,

- C. ESKILSSON, B. NELSON, P. VOS, C. BIOTTO, R. M. KIRBY, AND S. J. SHERWIN, *Nektar++: An open-source spectral/hp element framework*, Computer Physics Communications, 192 (2015), pp. 205–219, doi:10.1016/j.cpc.2015.02.008.
- [11] L. E. CARR III, C. F. BORGES, AND F. X. GIRALDO, *Matrix-free polynomial-based nonlinear least squares optimized preconditioning and its applications to discontinuous Galerkin discretizations of the Euler equations*, Journal of Scientific Computing, 66 (2016), pp. 917–940, doi:10.1007/s10915-015-0049-9.
- [12] M. O. DEVILLE, P. F. FISCHER, AND E. H. MUND, *High-order methods for incompressible fluid flow*, vol. 9, Cambridge University Press, 2002.
- [13] J. DONGARRA, I. DUFF, M. GATES, A. HAIDAR, S. HAMMARLING, N. HIGHAM, J. HOGG, P. V. LARA, M. ZOUNON, S. RELTON, AND S. TOMOV, *A proposed api for batched basic linear algebra subprograms*, tech. report, University of Tennessee, 2016. <https://bit.ly/batched-blas>.
- [14] P. F. FISCHER, S. KERKEMEIER, ET AL., *Nek5000 Web page*, 2017. <https://nek5000.mcs.anl.gov>.
- [15] G. HAGER AND G. WELLEIN, *Introduction to High Performance Computing for Scientists and Engineers*, CRC Press, Boca Raton, 2011.
- [16] A. HEINECKE, G. HENRY, AND H. PABST, *LIBXSMM: A high performance library for small matrix multiplications*, 2017. <https://github.com/hfp/libxsmm>.
- [17] M. A. HEROUX, R. A. BARTLETT, V. E. HOWLE, R. J. HOEKSTRA, J. J. HU, T. G. KOLDA, R. B. LEHOUCQ, K. R. LONG, R. P. PAWLOWSKI, E. T. PHIPPS, A. G. SALINGER, H. K. THORNQUIST, R. S. TUMINARO, J. M. WILLENBRING, W. A., AND K. S. STANLEY, *An overview of the Trilinos project*, ACM Transactions on Mathematical Software, 31 (2005), pp. 397–423, <http://www.trilinos.org>.
- [18] M. A. HEROUX ET AL., *Trilinos Web page*, 2017. <http://www.trilinos.org>.
- [19] J. S. HESTHAVEN AND T. WARBURTON, *Nodal Discontinuous Galerkin Methods: Algorithms, Analysis, and Application*, vol. 54 of Texts in Applied Mathematics, Springer, 2008.
- [20] F. HINDENLANG, G. GASSNER, C. ALTMANN, A. BECK, M. STAUDENMAIER, AND C.-D. MUNZ, *Explicit discontinuous Galerkin methods for unsteady problems*, Computers & Fluids, 61 (2012), pp. 86–93.
- [21] I. HUISMANN, J. STILLER, AND J. FRÖHLICH, *Factorizing the factorization – a spectral-element solver for elliptic equations with linear operation count*, Journal of Computational Physics, 346 (2017), pp. 437–448, doi:10.1016/j.jcp.2017.06.012.
- [22] INTEL CORPORATION, *Intel 64 and IA-32 Architectures Optimization Reference Manual*, July 2017. Order no. 248966-037, <https://www.intel.com/content/dam/www/public/us/en/documents/manuals/64-ia-32-architectures-optimization-manual.pdf>.
- [23] J. JEFFERS, J. REINDERS, AND A. SODANI, *Intel Xeon Phi Processor High Performance Programming, Knights Landing edition*, Morgan Kaufmann, Cambridge, MA, 2016.
- [24] G. E. KARNIAKAKIS AND S. J. SHERWIN, *Spectral/hp element methods for computational fluid dynamics*, Oxford University Press, 2nd ed., 2005.
- [25] A. KLÖCKNER, *Loo.py: transformation-based code generation for GPUs and CPUs*, in Proceedings of ARRAY ‘14: ACM SIGPLAN Workshop on Libraries, Languages, and Compilers for Array Programming, Edinburgh, Scotland., 2014, Association for Computing Machinery, doi:10.1145/2627373.2627387.
- [26] A. KLÖCKNER, T. WARBURTON, J. BRIDGE, AND J. S. HESTHAVEN, *Nodal discontinuous Galerkin methods on graphics processors*, Journal of Computational Physics, 228 (2009), pp. 7863–7882.
- [27] T. KOLEV ET AL., *MFEM: Modular finite element methods*, 2017. mfem.org.
- [28] D. KOMATITSCH ET AL., *SPECFEM 3D cartesian user manual*, tech. report, Computational Infrastructure for Geodynamics, Princeton University, CNRS and University of Marseille, and ETH Zürich, 2015.
- [29] D. KOPRIVA, *Implementing spectral methods for partial differential equations*, Springer, Berlin, 2009.
- [30] K. KORMANN, *A time-space adaptive method for the Schrödinger equation*, Communications in Computational Physics, 20 (2016), pp. 60–85.
- [31] K. KORMANN AND M. KRONBICHLER, *Parallel finite element operator application: Graph partitioning and coloring*, in Proceedings of the 7th IEEE International Conference on eScience, 2011, pp. 332–339.

- [32] B. KRANK, N. FEHN, W. A. WALL, AND M. KRONBICHLER, *A high-order semi-explicit discontinuous Galerkin solver for 3D incompressible flow with application to DNS and LES of turbulent channel flow*, *Journal of Computational Physics*, 348 (2017), pp. 634–659, doi:10.1016/j.jcp.2017.07.039.
- [33] M. KRONBICHLER, A. DIAGNE, AND H. HOLMGREN, *A fast massively parallel two-phase flow solver for the simulation of microfluidic chips*, *International Journal on High Performance Computing Applications*, (2016), in press, doi:10.1177/1094342016671790.
- [34] M. KRONBICHLER AND K. KORMANN, *A generic interface for parallel cell-based finite element operator application*, *Computers & Fluids*, 63 (2012), pp. 135–147.
- [35] M. KRONBICHLER, K. KORMANN, I. PASICHNYK, AND I. ALLALEN, *Fast matrix-free discontinuous Galerkin kernels on modern computer architectures*, in *ISC High Performance 2017*, LNCS 10266, J. M. Kunkel, R. Yokota, P. Balaji, and D. E. Keyes, eds., 2017, pp. 237–255, doi:10.1007/978-3-319-58667-0_13.
- [36] M. KRONBICHLER, S. SCHOEDER, C. MÜLLER, AND W. A. WALL, *Comparison of implicit and explicit hybridizable discontinuous Galerkin methods for the acoustic wave equation*, *International Journal for Numerical Methods in Engineering*, 106 (2016), pp. 712–739, doi:10.1002/nme.5137.
- [37] M. KRONBICHLER AND W. A. WALL, *A performance comparison of continuous and discontinuous Galerkin methods with fast multigrid solvers*, arXiv preprint, arXiv:1611.03029 (2016).
- [38] F. LUPORINI, D. A. HAM, AND P. H. J. KELLY, *An algorithm for the optimization of finite element integration loops*, *ACM Transactions on Mathematical Software*, 44 (2017), pp. 3:1–3:26, doi:10.1145/305494.
- [39] R. E. LYNCH, J. R. RICE, AND D. H. THOMAS, *Direct solution of partial difference equations by tensor product methods*, *Numerische Mathematik*, 6 (1964), pp. 185–199.
- [40] D. A. MAY, J. BROWN, AND L. LE POURHET, *pTatin3D: High-performance methods for long-term lithospheric dynamics*, in *Supercomputing (SC14)*, J. M. Kunkel, T. Ludwig, and H. W. Meuer, eds., New Orleans, 2014, pp. 1–11.
- [41] A. T. T. MCRAE, G.-T. BERCEA, L. MITCHELL, D. A. HAM, AND C. J. COTTER, *Automated generation and symbolic manipulation of tensor product finite elements*, *SIAM Journal on Scientific Computing*, 38 (2016), pp. S25–S47.
- [42] A. MODAVE, A. ST-CYR, AND T. WARBURTON, *GPU performance analysis of a nodal discontinuous Galerkin method for acoustic and elastic models*, *Computers & Geosciences*, 91 (2016), pp. 64–76, doi:https://doi.org/10.1016/j.cageo.2016.03.008, <http://www.sciencedirect.com/science/article/pii/S0098300416300668>.
- [43] S. A. ORSZAG, *Spectral methods for problems in complex geometries*, *Journal of Computational Physics*, 37 (1980), pp. 70–92.
- [44] A. T. PATERA, *A spectral element method for fluid dynamics: Laminar flow in a channel expansion*, *Journal of Computational Physics*, 54 (1984), pp. 468–488, doi:10.1016/0021-9991(84)90128-1.
- [45] F. RATHGEBER, D. A. HAM, L. MITCHELL, M. LANGE, F. LUPORINI, A. T. T. MCRAE, G.-T. BERCEA, G. R. MARKALL, AND P. H. J. KELLY, *Firedrake: Automating the finite element method by composing abstractions*, *ACM Transactions on Mathematical Software*, 43 (2016), pp. 24:1–24:27, doi:10.1145/2998441.
- [46] J. REINDERS, *Intel Threading Building Blocks*, O’Reilly, 2007.
- [47] J. SCHÖBERL, *C++11 implementation of finite elements in NGSolve*, Tech. Report ASC Report No. 30/2014, Vienna University of Technology, 2014.
- [48] S. WILLIAMS, A. WATERMAN, AND D. PATTERSON, *Roofline: An insightful visual performance model for multicore architectures*, *Communications of the ACM*, 52 (2009), pp. 65–76, doi:10.1145/1498765.1498785.